Aalto University
School of Chemical
Engineering

Tiia Tervamäki

LABEL-FREE SIZE-BASED RARE CELL SEPARATION BY MICROFLUIDICS

Master´s Programme in Chemical, Biochemical and Materials Engineering
Major in Functional Materials

Master's thesis for the degree of Master of Science in Technology submitted for inspection, Espoo, 27th of May, 2019.

Supervisor Professor Sami Franssila

Instructor Ph.D. Ville Jokinen
Ph.D. Anand Tatikonda

Author Tiia Tervamäki

Title of thesis Label-Free Size-Based Rare Cell Separation by Microfluidics

Degree Programme Master´s Programme in Chemical, Biochemical and Materials Engineering

Major Functional Materials

Thesis supervisor Prof. Sami Franssila

Thesis advisor(s) / Thesis examiner(s) Ph.D. Ville Jokinen and Ph.D. Anand Tatikonda

Date 27th of May, 2019 **Number of pages** 80 **Language** English

Abstract

Separating and isolating rare cells with cheap methods and rapid prototyping is attractive in analysing DNA in foetal cells circulating in maternal blood with non-invasive methods. Inertial microfluidics as a separation method is based on equilibrium points or trajectories that the particles migrate during flow. In this work, three different separation devices and one with a main purpose is concentration of diluted solutions after separation were investigated. The purpose of the thesis is to gain inertial focusing and particle separation.

The chips were fabricated by using soft-lithography process with SU-8 masters for transferring patterns on PDMS. After curing, the chips were cut, punched and treated with oxygen plasma to bond on microscope slides. Flow thru the devices was produced with syringe pumps. Devices were optimized first using de-ionized water, then investigated with different concentrations of polystyrene microparticles and finally with cells to gain preliminary results. Devices were tested within 0.006 ml/min to 10 ml/min range.

Non-equilibrium inertial array chip (NISA chip) is based on wall induced inertial lift force and siphoning by geometry induced pressure difference. NISA chip was investigated to separate 8 µm from 10 µm particles. The device had optimization issues with back-flow to feed, particle attachment to islands and low concentration of output samples.

Spiral chip is based on net inertial lift forces and Dean secondary flow induced by curvature of the device. The device was investigated with large throughput (above 4.9 ml/min flow rate) to separate 10 µm particles from 15 µm particles. Spiral chip had suboptimal outlet design, which let to large deviation in data. However, the results showed particle focusing during videoing of the flow although with low separation efficiency.

Labyrinth chip is likewise based on net inertial forces and Dean secondary flow as well as alternating corner design that induces additional mixing of particles. The chip was investigated with reasonably high throughput (above 1.75 ml/min flow rate) to separate 10 µm particles from 15 µm particles. The device showed inertial focusing both in video results and the particle analysis. Separation was seen in particle analysis.

Concentrator chip is based on inertial focusing and siphoning. Chip was investigated to concentrate solution of 10 µm 10^5 particles/ml tenfold. The device showed effective concentration using optimal flow rate with particles and using slightly slower flow rate with preliminarily cell experiments.

Keywords Inertial Microfluidics, Cell separation, Label-free, Size-based separation

Tekijä Tiia Tervamäki

Aalto-yliopisto
Kemian tekniikan korkeakoulu

Aalto Yliopisto, PL 11000, 00076 AALTO
www.aalto.fi

Diplomityön tiivistelmä

Työn nimi Harvinaisten merkkaamattomien solujen kokoon perustuva erottelu mikrofluidistiikalla

Tutkinto-ohjelma Master´s Programme in Chemical, Biochemical and Materials Engineering

Pääaine Functional Materials

Työn valvoja Prof. Sami Franssila

Työn ohjaaja(t) / Työn tarkastaja(t) FT Ville Jokinen and FT Anand Tatikonda

Päivämäärä 27 toukokuuta, 2019 **Sivumäärä** 80 **Kieli** Englanti

Tiivistelmä

Harvinaisten solujen erottelu ja eristäminen edullisilla menetelmillä ja nopealla prototypoinnilla on houkuttelevaa, kun analysoidaan verenkierrossa olevia kasvainsoluja tai DNA:ta sisältäviä sikiönsoluja äidin verestä ei-invasiivisesti. Inertiaalinen mikrofluidistiikka erottelumenetelmänä perustuu erikokoisten solujen taipumukseen asettua eri tasapainopisteisiin tai lentoradoille virtauksessa. Tässä työssä kolme erottelulaitetta sekä yksi solujen konsentrointiin erottelun jälkeen tähtäävä laite tutkittiin, jotta selvitettäisiin laitteiden kyky fokusoida ja erotella partikeleita.

Sirut valmistettiin pehmyt-litografialla, jossa SU-8 mastereilla siirrettiin mikrofluidistiset kanavat PDMS:ään. Kovettumisen jälkeen sirut leikattiin, rei'itettiin, käytettiin happiplasmassa ja bondattiin mikroskooppilaseihin. Virtauskokeissa käytettiin ruiskupumppua. Laitteet tutkittiin ja optimoitiin alustavasti ensin deionisoidulla vedellä ja sitten erilaisilla polystyreeni mikropartikkeli liuoksilla ja lopuksi vielä alustavilla solukokeilla. Laitteet tutkittiin virtausnopeusvälillä 0.006 ml/min - 10 ml/min.

Inertiaaliarray siru (NISA siru) perustuu kanavan saarien seinien aiheuttamaan inertiaalivoimaan ja lappoon, joka syntyy geometriasta johtuvista paine-eroista. Laite tutkittiin tarkoituksena erottaa 8 µm partikkelit 10 µm partikkeleista. Laitteen optimointi osoittautui haasteelliseksi johtuen nesteen takaisinvirtauksesta syötteeseen, partikkelien tarttumisesta saariin ja ulostulojen matalasta konsentraatiosta.

Spiraali siru perustuu inertiaalivoimiin ja Deanin sekundaari virtauksiin, jotka johtuvat kanavan kaareutuvuudesta, sekä kanavan pylväiden virtausta supistavaan vaikutukseen. Laite tutkittiin korkeilla virtausnopeuksilla tarkoituksena erottaa 10 µm partikkelit 15 µm partikkeleista. Spiraali sirun ulostulon design aiheutti korkeaa hajontaa partikkelianalyysissa. Toisaalta, laitteen virtauksen videotuloksissa ja partikkelianalyysissa on nähtävissä selkeä inertiaalifokusointi.

Labyrintti siru perustuu myös inertiaalivoimiin ja Deanin sekundaari virtoihin sekä laitteen designissa olevien kulmien partikkeleita sekoittavaan vaikutukseen. Laite tutkittiin korkeahkoilla virtausnopeuksilla keskittyen 10 µm ja 15 µm partikkelien erotteluun. Laitteen virtauksen videotuloksissa ja partikkelianalyysissa on selkeä fokusointi. Lisäksi erottelua oli havaittavissa partikkelianalyysissa.

Konsentraattori siru perustuu inertiaalifokusointiin ja lappoon. Laite tutkittiin tarkoituksena konsentroida 10 µm 10^5 partikkelia/ml kymmenkertaisesti. Laitteessa oli havaittavissa selkeää konsentroitumista partikkeleilla optimaalisella virtausnopeudella ja alustavissa solukokeissa hieman matalammalla virtausnopeudella.

Avainsanat Inertiaalinen microfluidistiikka, solujen erottelu, markkeeriton, kokoon perustuva erottelu

Definitions

Concentrator chip is inertial microfluidic device that aims to concentrate solution by inertial focusing and siphoning.

d is particle diameter

De is Dean flow strength or Dean number

D_h is the hydraulic radius of the channel

DIW is De-ionized water

EMEM is Eagle's Minimum Essential Medium

F_D is Dean drag force

F_L is lift force

f_L is lift coefficient

$\vec{F}_{LR}$ is the Magnus' lift force

$\vec{F}_S$ is the Saffman lift force

H is channel height

Labyrinth chip is inertial microfluidic serpentine type device that resembles a labyrinth and is based on inertial forces, Dean secondary flow and mixing by sharp corners.

NISA Chip is Non-equilibrium inertial separation array that is based on inertial wall induced lift force and siphoning.

p is the fluid pressure

PBS is Phosphate-buffered saline

PDMS is Polydimethylsiloxane

PS is Polystyrene

R is the radius of the curvature

Re_c is channel Reynolds number

Re_p is the particle Reynolds number

R_f is the ratio between inertial lift force and Dean drag force

SDS is Sodium Dodecyl Sulphate

Spiral chip is inertial microfluidic spiral design with ridges. It is based on inertial lift forces, Dean secondary flows and expansion-contraction induced by ridges.

SU-8 is epoxy-based negative photoresist

SU-8 master or master is master silicon wafer that has microfluidic design pattern fabricated with SU-8 photoresist and treated with fluorine plasma

$\vec{u}$ is the fluid velocity vector

U_D is the transverse velocity

U_m the maximum flow velocity in the channel

V_f is the volume fraction of particles in solution

W is the channel width

Greek alphabet

δ is curvature ratio

λ is the ratio that predicts single stream focusing

μ is the dynamic viscosity of the fluid

ρ is density of fluid

$\vec{\Omega}$ is the angular velocity

Acknowledgements

I want to thank Leppä, M., Eskelinen, P. and Mannerkoski, T. for excellent team work during Group Research Assignment -course at Aalto University autumn 2017. The course was a beginning for this thesis.

I would like to express my gratitude to V. Jokinen, A. Tatikonda, professor S. Franssila and the research group of Microfabrication for all the support given during the thesis.

I am grateful for the thesis project, collaboration, providing the cells and overall support given by M. Sairainen, V. Veikkolainen, J-P. Kakko and Perkin Elmer.

I acknowledge the help of H. Honkala for device holder and chats, C. Jonkergouw for instructions for optical microscopy, M. Kärkkäinen for Laser diffraction measurement instructions.

I give a warm appreciation to K. Yliniemi for the support throughout my Master degree studies in Functional Materials.

The experiments for this thesis were undertaken at the Micronova Nanofabrication Centre of Aalto University.

Table of Contents

1 Introduction

Label-free size-based cell separation by microfluidics aims to separate rare cells from a vast number of cells in blood by size without affinity-based labels. Label-free methods rely on physical difference in properties such as size, shape or polarizability, whereas labelling is based on differences between cell surface markers and fluorescent staining. Traditionally rare cell sorting has been commercially done by using label-based methods, flow cytometry and magnetic cell sorting, both of which have limitations with e.g. sample throughput, processing speed, bulky equipment, high sample processing costs and time, and safety using aerosolized samples (1).

With microfluidic cell sorting the size of the equipment can be reduced, biohazardous aerosols eliminated, and complex processing protocols of cells simplified (2). Additional benefits are reduced sample sizes, improved portability, high sensitivity and ability to be integrated and automated. Microfluidic chip that uses mainly passive inertial forces is a size-selective, non-invasive and faster than most active sorting methods and methods that require long pre-processing of samples to enrich the larger rare cells. Microfluidics offers a method to separate cells that is less expensive and time-consuming as traditional methods, especially when the surface markers of the wanted cells are unknown.

Microfluidics can be used for cell separation, because it can in a reasonable manner be operated in size ranges matching cell sizes. Blood cells range from platelets (2 - 3 µm (3)), red blood cells (7 - 8 µm (4)) to white blood cells (10 - 20 µm (5)). Rare cells are usually in the size approximately range of 9 – 19 µm for CTCs (but also less than 10 µm and larger than 30 µm) (6), 12 - 16 µm for circulating trophoblasts in blood and 12 – 40 µm for trophoblast sample from placenta (7). The aim is to enrich the desirable cells to a reduced volume of sample that is then analysed further with e.g. optical microscopy, while recovering all the rare cells and keeping carryover of other cells minimal.

We investigate microfluidic chips in this thesis, with the focus in mind to separate trophoblasts from pregnant women's blood. During pregnancy, mother's and foetus's health is monitored to detect early on any anatomic and physiological problems. Currently, foetus's DNA can be obtained with invasive methods (amniocentesis and chorionic villus test) and with non-invasive methods to collect foetus's DNA from maternal blood (8). There are two types of collecting the foetus's DNA from blood; the viable cells (e.g. trophoblasts) and the circulating cell-free DNA. With cfDNA, it is harder to differentiate the foetus's DNA from the maternal DNA. Furthermore, the major benefit of analysing viable cells is that the whole genomic DNA remains intact. It is proven that even the first trimester blood samples of a pregnant women contain foetal cells and moreover they are mainly mononuclear. In this work, we focus on trophoblasts due to their size difference from abundant blood cells. However, the count of these cells originating from placenta is reportedly only five cells per ml.

Four different microfluidic chips that mainly use inertial forces to separate cells were evaluated in this thesis. These designs were selected from peer reviewed articles and the purpose of the thesis is to gain proof-of-concept results and understanding of separation of rare cells with inertial microfluidics. Three of the devices are focused on enrichment of rare cells from diluted blood and one of the devices is focused on re-concentration of diluted solutions.

The chips were mainly operated with polystyrene microparticles due to access, ease and comparability to cells by size. Our testing included microparticles with 8, 10 and 15 µm sizes in solutions of 0.1 and 1 million particles per ml. Additionally, cells were investigated with alternating concentrations from 10^3 to 10^5 cells per ml both in EMEM and PBS solutions. Cell size of the tested cell were approximately 10 to 40 µm. The preliminary cell experiments were in line with literature results. All four chips were successfully evaluated and three of the chips were proven to be fulfilling their promises that were given by the articles.

2 Cell Separation by Microfluidics

There are multiple different approaches to separate cells or DNA from blood. Earlier work has been done sorting various cell lines of circulating tumor cells (CTCs), cell free DNA (cfDNA), foetal nucleated RBCs (nRBCs) and trophoblasts. The foetal cells identified from circulating maternal blood are suggested to be extravillous trophoblasts (9). The trophoblasts are in the range of 1-5 cells per ml (10), while RBCs are in the range of $5*10^9$ cells per ml, platelets $4*10^8$ cells per ml and WBCs $7*10^6$ per ml. The problem then becomes of retrieving all the rare cells from the abundant amount of host cells.

We selected label-free size-based inertial microfluidics, because it has major benefits in high throughput, simplicity, robustness and ease of parallelisation and fabrication (11). Label-free size-based inertial microfluidics has been studied in extraction of blood plasma, separation of particles and cells, solution exchange, cell enrichment, isolating CTCs, detecting the malaria pathogen, cell cycle synchronisation, cell encapsulation and hydrodynamic stretching of single cells. While the geometry is somewhat limiting in inertial microfluidics, it can be overcome with precise design and fabrication of the device, optimization of the operation and, parallelization and serialization. Separation resolution has additionally some inaccuracies, when compared to active methods such as optical cell-by-cell type manipulation.

2.1 Fabrication

Manufacturing of microfluidic chips are done with microfabrication methods in which the soft-lithography is common in microfluidics. Microfabrication have advantages in on-chip separation: 1. high surface area to volume ratio, 2. modulation of fluidic flow characteristics 3. sizes of cells (8 – 50 µm) match the dimensions of channels (1 – 1000 µm) and length of devices (1 – 1000 mm) (12). Additionally, rapid prototyping with PDMS on glass is effective method to gain proof-of-concept in microfluidics.

2.2 Foetal DNA analysis

The foetal DNA is required to be analysed before early pregnancy to detect abnormalities. Non-invasive prenatal testing (NIPT) methods are based on separation and analyses of DNA from circulating cfDNA and intact foetal cells from 7 ml of peripheral maternal blood (8).

Even though extraction and analysis of cfDNA from maternal blood is available, the net results of cell-free NIPT analysis has been that there are more infants with disabilities than found by using cfNIPT (8). Nevertheless, the cfNIPT has revolutionized the field with non-invasiveness. It still remains limited to aneuploidy and microdeletion screening, but not to detect single gene disorders (13). Thus, intact DNA from cells can offer more reliable results.

Foetal cells circulating in maternal blood are nucleated RBCs and trophoblasts (8). The foetal nRBCs are difficult to differentiate from maternal RBCs, due to their similar properties. Although, they have been analysed with fluorescence in situ hybridization (FISH) to detect aneuploidy and sex. Better results have been gained with magnetic-based separation systems (MACS) than with the flow sorting in FACS. Most of the focus has been on nRBCs using positive enrichment by MACS with antibodies CD71 or FACS with antibodies to haemoglobin F (HbF). There have been many efforts using various combinations of MACS, FACS, density separation and high-throughput microscopic scanning, but also filtration based on cell size. The disadvantage with these methods is that they are complex, time-consuming and expensive.

Therefore, the benefit of separating trophoblasts from blood is the intact DNA and differentiation from abundant cells by size. Earlier work has been done to enrich trophoblasts from blood using antigens, by electrophoretic separation or charge flow separation (CFS), passing cells through a gradient (10) and with a serpentine type microfluidic chip (14). Additionally, fluorescence-activated cell sorting (FACS) is used to enrich foetal cells using antibody HLA-2 labelling and staining to detect the cells with microscopy (8).

2.3 Microfluidic cell separation

Cell separation by microfluidics can be classified in active and passive technologies (1). In active methods an external field such as acoustic, electric, magnetic and/or optical manipulates the cells, while passive methods rely on inertial forces, filters and adhesion. Additionally, separation technologies can be organized into fluorescent label-based, bead-based and label-free sorting by the primary cell recognition modality.

Alternatively, the microfluidics separation technologies can be defined as affinity-based and physical force-based approaches (12). Affinity-based technologies take advantage of cell surface markers and affinity ligands, i.e. antibodies and aptamers, and the noncovalent bond forming between them. When cells resemble physically each other, but have differences in surface markers, this method is feasible. Antibody-based methods can be classified as immunocytochemistry (ICC), immunomagnetic and adhesion-based methods. Physical force-based or label-free based technologies rely on separation by cell structure properties such as size, deformability and density.

2.4 Label-based and bead-based

Labelling is done by attaching a fluorescent marker on cell surface. The cell has surface sites that bind antigens that are tagged with conjugates of antibodies (15) or proteins with fluorophores (16). The labelling is bound by immunological properties of cells and require not only the surface chemistry of target cell but also of host cells (15).

A material with the property of fluorescence absorbs light and re-emits that with longer wavelength (16). Most cells do not have intrinsic fluorescence and they need to be labelled. Multi-labelling analysis has several practical problems; antibodies bind to other than to the target antigen, they adhere non-specifically or form aggregates.

In bead-based technologies the cells are introduced with beads that have specific material, size or surface affinity (1). They are used to capture target or non-target cells and sorted out with external field. It does not require serial interrogation of cells and groups of cells can be manipulated at the same time. Thus, the sorting can have potentially faster rates and smaller volumes of diluent than in label-based. The methods consist magnetophoresis, acoustophoresis and electrokinetic mechanisms. However, the throughput may remain small and there may be uneven distribution of beads to cells that influence efficiency and carryover.

In FACS the cells are organized in a laminar flow stream and they encounter a focused laser beam that scatters into a detector (16). Fluorescent signal in analysed to assign each cell to a discrete sorting; e.g. cell is encapsulated into a charged aerosol droplet and sorted electrostatically. Similar methods to FACS are serial interrogation by laser light, real-time classification and rapid command-driven sorting. Sorting is highly efficient. Immunostaining assays are ubiquitous, reliable and require less preparation time than bead-based labelling, which can help reduce experimental error. Some label-based methods can be attached to FACS, e.g. electrokinetic, acoustic, optic and mechanical sorting (1). Problems with FACS are with serial detections, discrete sorting and that the labels do not directly contribute to the sorting.

2.5 Label-free cell sorting

Label-free technologies are the most used of the methods (1). They rely on physical differences in cell properties such as size, shape, density, elasticity, polarizability and magnetic susceptibility. Additionally, cells ability or preference to penetrate through membranes can be utilized. More target cell property information can help in designing a separation device, such as magnetic properties, density, flexibility, compressibility, desire to attach to different surfaces, etc. Earliest automated sorter was an impedance technique based on the Coulter principle. Label-free methods require the least amount of preparation and processing, and thus a highly attractive option.

2.6 Size-based sorting

Size-based microfluidics separates bioparticles by their size difference. In many methods the cells are induced by a force that migrates particles into different trajectories in the channel or flow stream. Isolation or trapping of single cells based on their size are not considered in this work.

Active methods require external force to sort out cells. These methods are acoustic, electric, magnetic and/or optical. In acoustophoresis acoustic waves migrate particles into different trajectories by size or compressibility (1). In electrokinetics; e.g. dielectrophoresis (DEP) uses intrinsic dielectric properties or size to separate, filter or concentrate cells. Field-flow fractionation (FFF) is commenly included to approaches such as DEP, gravitational, centrifugal, thermal and magnetic to displace cells. However, traditional DEP fabrication methods are expensive (18). Some electrokinetic such as electro-osmotic flow have a major set-back with Faradaic reactions in solutions (1). Magnetophoresis uses either magnetic nanoparticles to capture and isolate cells or cells intrinsic iron content, i.e. RBCs separation from other blood components. Additionally, diamagnetic cells are separated in ferrofluids by size, shape and deformability and in paramagnetic solutions by size. Optical methods include switches and tweezers. However, their major limitation is the sorting speed as the separation is done one-by-one with one laser. There are attempts to optoelectronically use tweezers sort cells by e.g. size and viability.

As before mentioned methods, acoustophoresis, DEP, magnetophoresis and optical methods can be used for size-based label-free cell sorting (11). Active methods offer possibility to control cells precisely and be adjusted in real time whereas passive methods offer easy manipulation and reliability with high throughput. The drawback of active methods is the slow flow rate and throughput due to long residual time needed for exposure to the field whereas passive methods have fixed designs that can be operated within limited range although parallelisation is moderately easy. Additionally, active methods need to overcome the hydrodynamic drag to be effective, which is limiting the

throughput (2). Passive methods are operated without dependence on an external field and rely on inherent differences in cellular morphology (1). Sorting occurs using inertial forces, pinched flow and hydrodynamic spreading, deterministic lateral displacement, filtration, sieves, hydrophoresis, or transient cellular adhesion and cellular immobilization.

Deterministic lateral displacement (DLD) uses micropatterns within the microfluidic channel to provide spatial manipulation to separate cells (17). Control over sorting is based on the gap between microcolumns and the column shift of adjacent rows. There exist two different migration modes; displacement and zigzag. The separation occurs if one particle size follows displacement and the other particle size the zigzag mode shown in Figure 1. DLD separation can be based on size, shape and deformability (1). DLD devices have disadvantages in not being able to process whole blood in high volumes due to cells interacting directly with pillars, spacing requirements to prevent yield losses of larger cells and clogging (18).

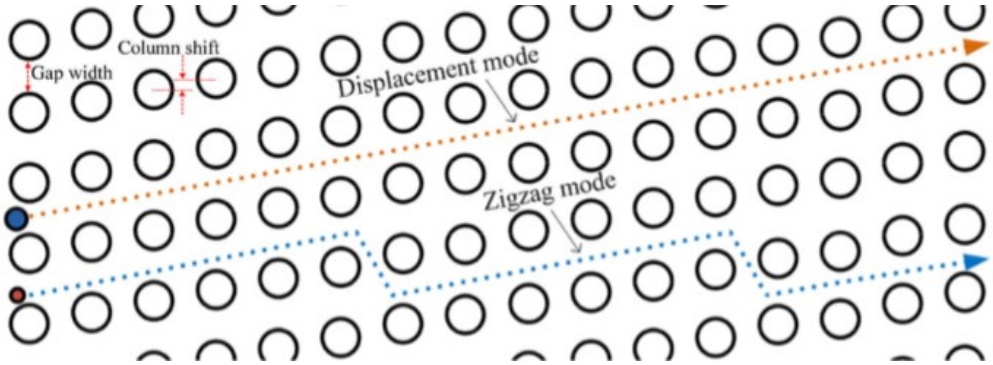

Figure 1 The two modes in DLD separation device (17)

Hydrophoresis is emerging technique, where steric effects between particles and grooves are utilized (1). Hydrophoretic filtration is ridge-induced and relies on formation of lateral pressure gradient within channel due to flow-altering micropatterns. Accurately fabricated designs of arrays can induce a pressure field that focus, guide and sort cells to precisely. Basis for separation can be size, deformability and density. Size exclusion filtration refers to posts with tiered spacing as a function of distance. It includes series of linear arrays of pillars that selectively group cells by size and shape. Some earlier filter designs

such as weir filters, pillar filters and membrane filters were used to trap cells (Figure 2a, b and d) (19). Cross-flow or tangential flow filtration use an array of lateral slits in direction of flow to fractionate by size (Figure 2c) (19) (20). Behaviour of cross-flow filters is more like a sieve than dead-end filter. Hydrodynamic filtration separates cells, when fluid is drained from multiple branched outlets. Major draw-back of filters is clogging by larger cells or depris.

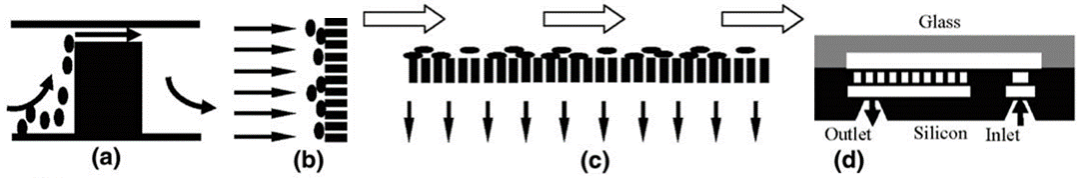

Figure 2 Filter types used for cell separation. a) weir filter, b) pillar filter, c) crossflow and d) a membrane filter. (19)

Pinched flow fractionation and hydrodynamical spreading happens, when flow stream is pinched in a narrow channel, where cells are constrained and aligned against wall (21) (22). Then, spreading of the channel separates the cells by the laminar flow profile deterministically (Figure 3). Sheath flow, asymmetric design and gravitational forces enhance the sorting.

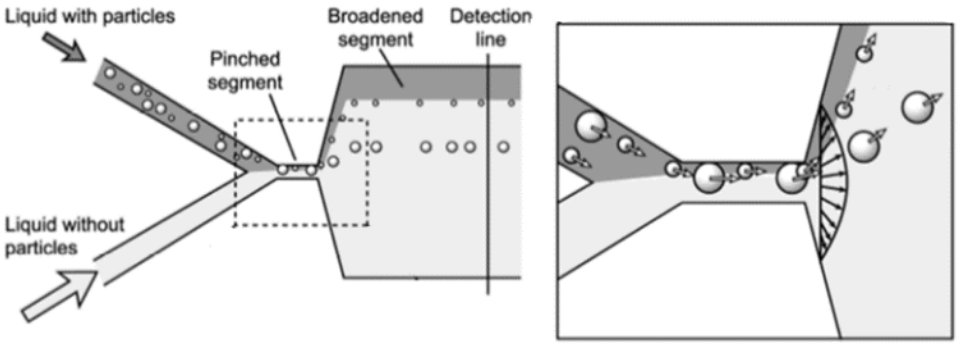

Figure 3 Particle trajectories change deterministically in pinched flow fractionation. The smaller particles remain near to wall, while larger focus near centreline after hydrodynamical spreading (21).

Transient cellular adhesion or cellular immobilization is traditionally based on cell surface chemistry (1). However, physical properties are utilized as well, for example CTCs have a different adhesion preference to nanoroughened surfaces than blood cells (23). Additionally, the forces of transient cellular adhesion might be miniscule and require low flow rates (1).

Inertial focusing is a phenomenon, where inertial forces induce lateral migration of cells in laminar flow streams (24). Fluid flow adjacent to walls experience boundary effects that cause lift. In channel with curvature, asymmetry or expansion-contraction areas arise Dean secondary flow that enhance the focusing. A major benefit of inertial focusing is the high throughput or sequential cell manipulation aiding the processing of native biological fluids and flow cytometry. Inertial focusing is discussed further in Chapter 3.

2.7 Hybrid Mechanisms

Separation of rare cells with one microfluidic method is proven to be difficult from complex and homogeneous native fluid (11). Hybrid microfluidics can process multi-target cells, enhance multiplexed separation and has higher sensitivity and tuneable operation for wider range. Both active and passive methods have their limitations that can be reduced with hybrid methods of active-active, passive-passive or active-passive combinations. For example, incorporation of multiple methods has been successfully done using inertial focusing between deterministic lateral displacement and magnetic sorting (6). CTC-ichip is a high throughput device; 10^7 cells/s or 8 ml/h (= 0.133 ml/min) with flow rate between 50 and 150 µl/min.

Other successful example of hybrid passive-passive design uses cell size and deformability as separation and enrichment basis using multistage microfluidic device with filtration, inertial focusing and separation regions, and steric hindrance (Figure 4). From diluted blood Shen et al (20) were able to recover over 90 % at $2.24*10^7$ cells/min with $2.02*10^5$-fold enrichment.

Combining both active and passive method brings the benefits of both but also the drawbacks (11). The problem of hybrid microfluidics is combining components in series with independent physics or parallel with coupled physics. For example, passive microfluidics such as inertial microfluidics uses high flow rate, whereas an active method requires significantly slower rate. Additionally, the interface in between needs to be designed and balanced

carefully, so that the downstream section works properly. For example, the physiological medias do not work well with DEP due to osmotic pressure suitable for viability and conductivity.

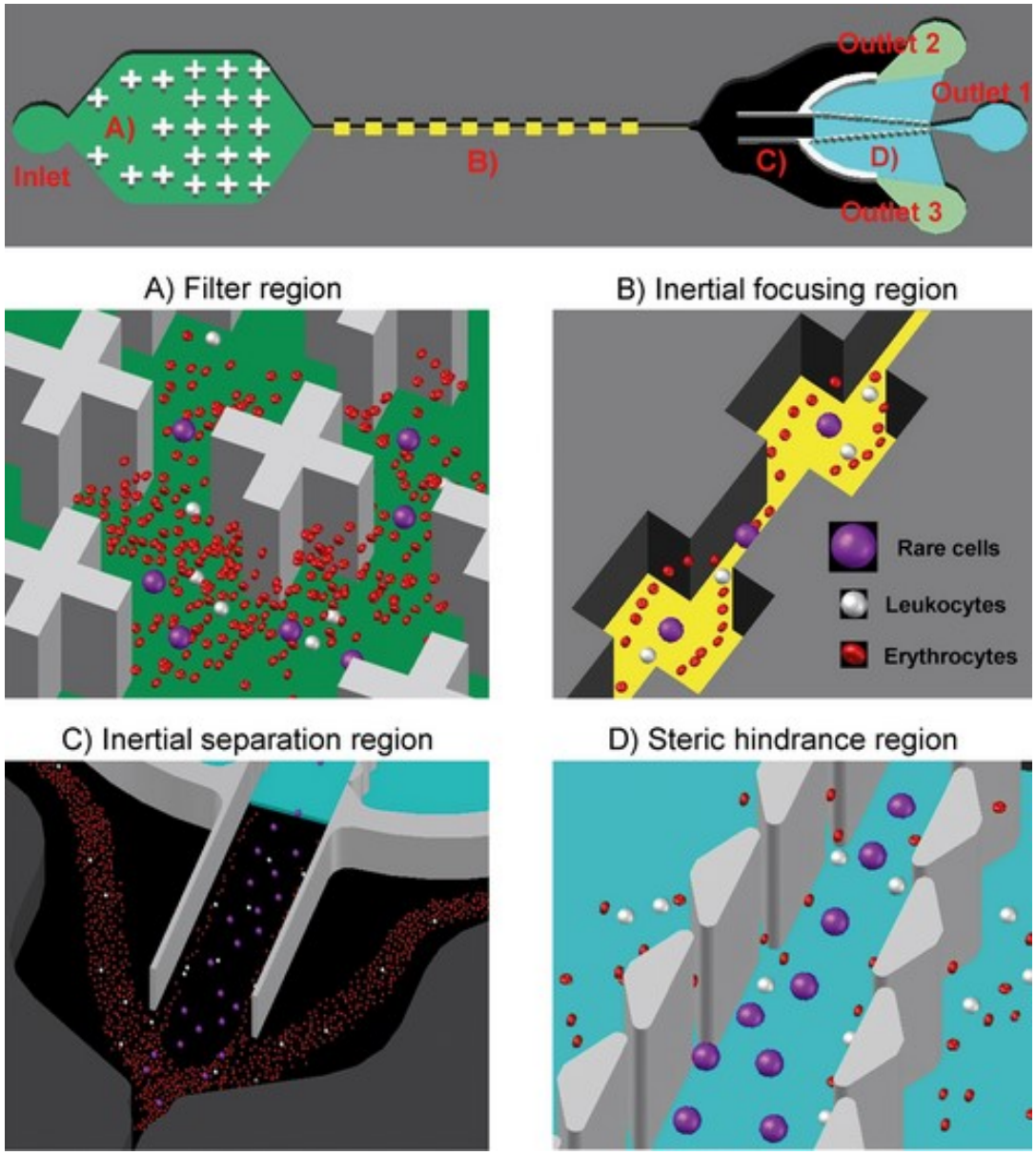

Figure 4 Hybrid microfluidic device consists stepwise separation areas with passive physics-based enrichment of rare cells (20). First a pillar filter (A) separates rare cells from excess amount of blood cells. Then inertial focusing region (expansion-contraction type) or multi-orifice flow fractioning (B) focuses the larger rare cells near the centreline and the smaller blood cells near wall. Then these focused cells continue to deterministic trajectories, when the channel spreads to an inertial separation region (C). Finally, the steric hindrance region or the cross-flow filter (D) separates the smaller cells near wall by passing them through micropillars to waste, while larger cells continue to product.

3 Inertial Separation in Microfluidic Chips

In this chapter we discuss the phenomena of inertial focusing in microfluidic channels. Then we will describe the peer-reviewed inertial microfluidic chips replicated for proof-of-concept experimenting.

3.1 Inertial migration in microfluidic channels

Microfluidic channels are coverned by Poiseuille flow that induces a parabolic flow profile, which makes possible the particle inertial focusing (14). The steady-state incompressible Navier-Stokes equation (1) and the continuity equation (2) describe fluid flow in a microfluidic channel.

$$\rho(\vec{u} \cdot \nabla)\vec{u} = -\nabla p + \mu\nabla^2\vec{u} \quad (1)$$

$$\nabla \cdot \vec{u} = 0 \quad (2)$$

Where ρ is density of fluid, μ is the dynamic viscosity of the fluid, $\vec{u}$ is the fluid velocity vector and p is the fluid pressure. Mathematically inertial focusing requires solving partial differential equations in equation (1) and (2), nonlinearity and both moving multiple boundaries (particles or cells), and complex three-dimensional boundaries (the channel geometry) (25). Simulations of these problems are time-consuming and thus far experimental research is faster in determining effective focusing channels.

In microfluidic channel, particles experience both inertial lift and viscous drag forces (20). Reynolds number is a dimensionless number that measures the ratio of inertial forces over viscous forces and it characterizes the fluid dynamic phenomenon. For a channel, Reynolds number is defined as

$$Re_c = \frac{U_m \rho D_h}{\mu} \quad (3)$$

Where U_m the maximum flow velocity in the channel, D_h is the hydraulic diameter of the channel and defined for a rectangular cross-section as

$$D_h = \frac{2HW}{H+W} \quad (4)$$

Where H is the channel height and W the channel width. Lift force that particle experiences has complicated reliance on geometry of the design, particle

diameter and the position of the particle between wall and the centreline (26). Lift is also changing with the change of Reynolds number. Higher Reynolds number induces lower lift near wall and increase in lift near centre.

Many microfluidic devices are operated in the laminar flow range and furthermore in the Stokes flow region $Re_c < 1$. However, the inertial microfluidics are operated in an intermediate flow region between Stokes and turbulent defined by Hood (25) as $1 \leq Re \leq 500$ and Zhang et al (2) as $1 \leq Re \leq 100$.

Motion of the particles can also be described with particle Reynolds number defined as (20)

$$Re_p = Re_c \frac{d^2}{D_h^2} = \frac{\rho U_m d^2}{\mu D_h} \quad (5)$$

where d is particle diameter. When the particle Reynolds number >> 1, the inertial lift is dominant in driving the lateral migration of particles transverse to the fluid streamlines. In addition, when $Re_p << 1$, the viscous drag force acting on the particle surface has an important role in driving longitudinal particle migration in the channel.

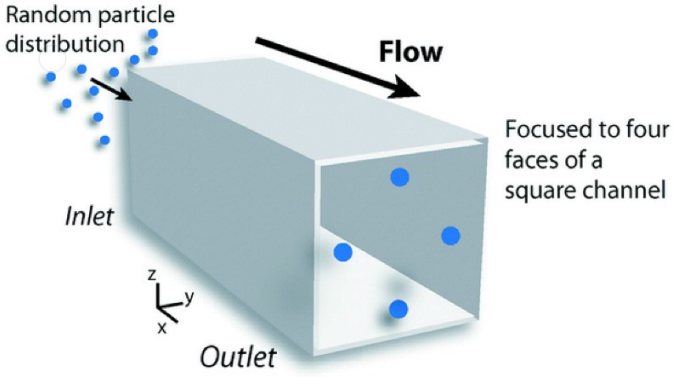

Figure 5 In square cross-sectional straight channel the inertial focusing migrates particles toward four dynamical equilibrium positions. (27)

Fluid inertia in inertial microfluidics is negligible or finite, but so is viscosity (2). Inertia being finite creates phenomena of inertial migration of the particles and secondary flow. In inertial migration dispersed particles migrate laterally in a channel to several equilibrium positions within flow (Figure 5). It occurs, when opposing forces find a balance within flow.

Lateral rigid particle migration in laminar flow across streamlines to equilibrium positions are defined by Di Carlo (24) as mathematically for a particle to occupy a stationary point in a dynamical system. Regardless of the size of the particle and equilibrium position, the particle velocity remains equal to each other (26). There are multiple forces acting on the particle during flow. Shear gradient induced lift force and wall effect induced lift force are thought to be first balancing out the particle into set number of equilibrium positions that are influenced significantly by the channel geometry (2). In channels with curvature, asymmetry or contraction-expansion region, a secondary flow arises. Other forces are believed to be negligible, i.e. Magnus' and Saffman forces. Additionally, diffusion occurs by Brownian random motion of the immersed particles in the fluid and it is considered negligible.

Shear gradient force is produced by the parabolic profile of Poiseuille flow that drives rigid particles toward walls as shown in Figure 6 (20). Shear rate has profound effect on lift. Finite shear gradient in cylinder shape channel or square channel is different than in a high aspect ratio channel (26). At the middle point of a rectangular channel, the shear gradient approaches zero and the wall directed shear gradient induced lift is eliminated. Thus, a high aspect ratio channel has lower number of equilibrium positions.

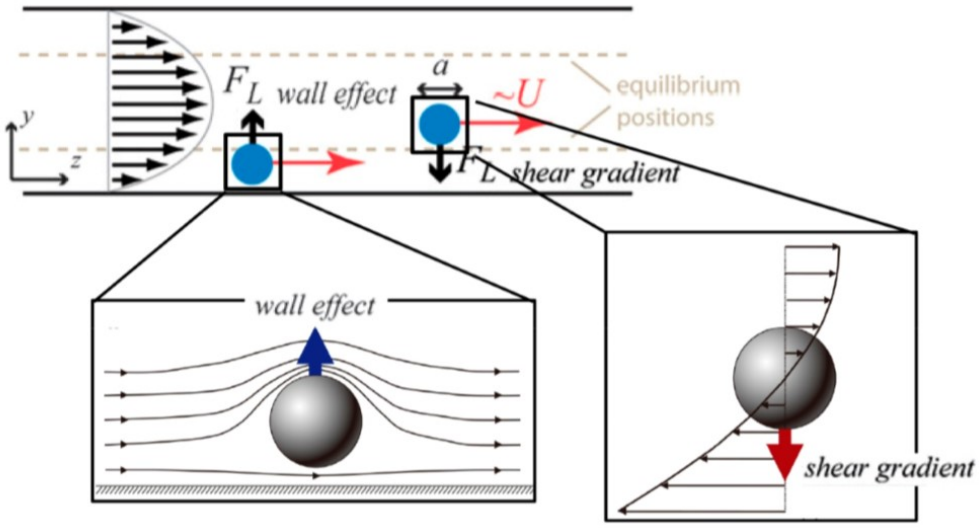

Figure 6 The Poiseuille flow profile causes a shear gradient that migrates particles toward wall and wall induced lift force lifts the particles toward the centreline (28).

When particles experience the shear gradient induced force, they migrate closer to the wall. Opposite force starts to counteract on the particles, because of fluid velocity and asymmetric wake vorticity generated at the surface of the rigid particles (Figure 6) (20). The vorticity is induced by a higher pressure near the wall side of the particle than on the centreline side. Zhang et al. (2) suggest that the walls also induce the rotation of particles. Walls effect the particle motion by deceleration it by drag and repelling the particles toward the centreline by lift force.

Magnus' force is due to slip-rotation of the particle (14). The rotation of the particle during flight in equilibrium positions was observed to be equal among same sized particles, dependent on particle size and decreasing with more confinement. However, Di Carlo et al. (26) suggested that the rotation was not contributing to lateral migration. While Zhang et al. (2) thought that rotation induced force is a lateral lift force that a rigid sphere rotating in a fluid experiences due to transverse pressure difference, induced by streamline asymmetry (Figure 7a). Additionally, Shen et al. (20) believes that rotation induced lift acts directionally generating net force toward the channel centre.

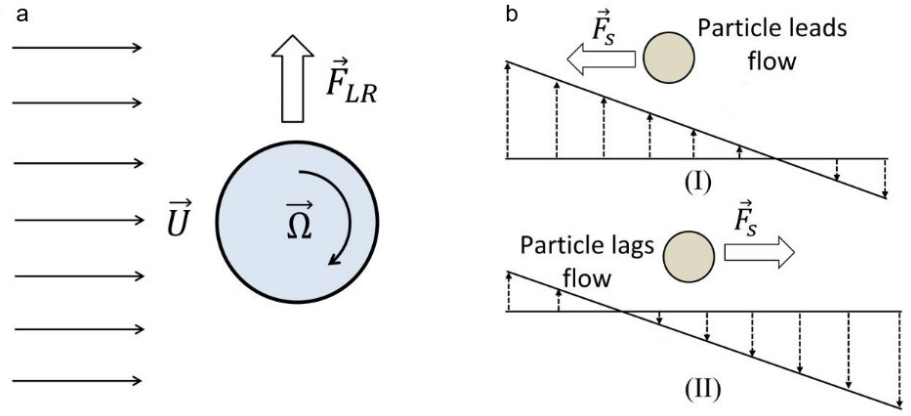

Figure 7 Magnus' rotational force (a), where $\vec{F}_{LR}$ is the Magnus' lift force, $\vec{\Omega}$ is the angular velocity and Saffman force (b) $\vec{F}_S$ is toward the centreline, when particle leads the flow (bI) and toward wall, when the particle lags flow (bII). (2)

Saffman force is slip shear induced lift force (2). Channel walls create the velocity gradient, and shear stress induced particle rotation. Drag from the walls cause particles to lag behind the flow (Figure 7). Additionally, walls

disturb the flow field around particles. Saffman arises from interaction between the Stokeslet velocity field of the particle and the velocity gradient of the bulk flow. Saffman is one order magnitude lower than Magnus' force in low Reynolds number flows. Saffman is more relevant to particles of non-neutrally buoyant, such as polystyrene particles in DIW, than neutrally buoyant particles. Direction is either laterally toward the wall or toward the centre depending on, if the particles lag or lead the flow (Figure 7).

Asmolov's (29) model describes the net inertial lift force that consists two major lift forces:
At near the centre:

$$F_L = \frac{f_L \rho U^2 d^4}{D_h^2} \quad (6)$$

At near the wall

$$F_L = \frac{f_L \rho U^2 d^6}{D_h^4} \quad (7)$$

Where f_L is lift coefficient and is commonly approximated averagely as 0.5 (2).

Asmolov's (29) model describes the wall-induced lift force decreasing as the particle migrates toward the centreline of a channel by the flow profile curvature. Theoretically wall-induced lift force vanishes at the centreline of a cylinder -shaped channel, but there is no equilibrium position at the centreline. Thus, the particles do not experience non-zero wall lift.

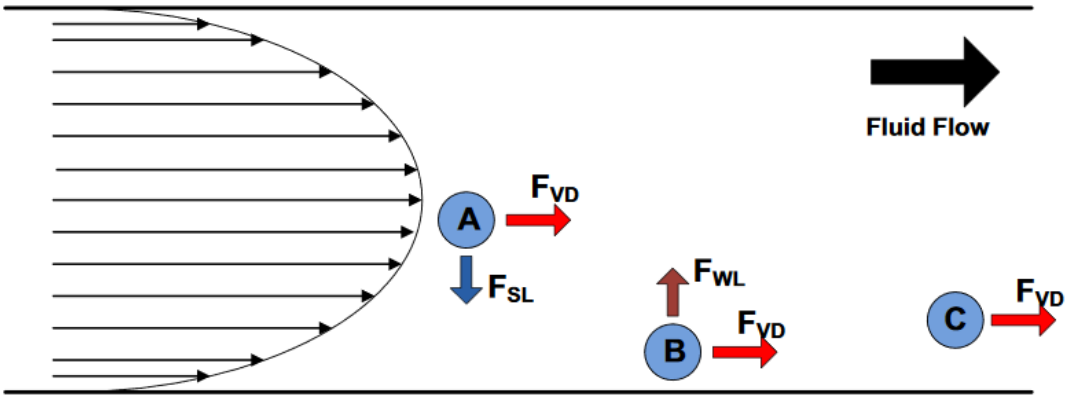

Figure 8 Main forces influencing the particle migration are shear-induced force (F_{SL}), wall induced lift force (F_{WL}) and viscous drag force (F_{VD}) (30).

In Figure 8, the two main lift forces in a straight channel are drawn. Particle experiences lift from shear-induced force toward wall and wall induced lift force toward centreline and the viscous drag force in the direction of the flow. In straight channels the inertial forces are enough to migrate particles (2). In channels were the secondary flow arises, it mixes and changes the equilibrium positions. In curved channel the secondary flow is induced by pressure gradient in radial direction. Fluid elements near the centre have higher momentum and they drive flow toward the stagnant elements near wall around circumference and create two counter-rotating Dean vortices (Figure 9). These can modify the equilibrium positions by adding additional viscous drag force to particles. Dean vortices can help reduce the length of the device with mixing.

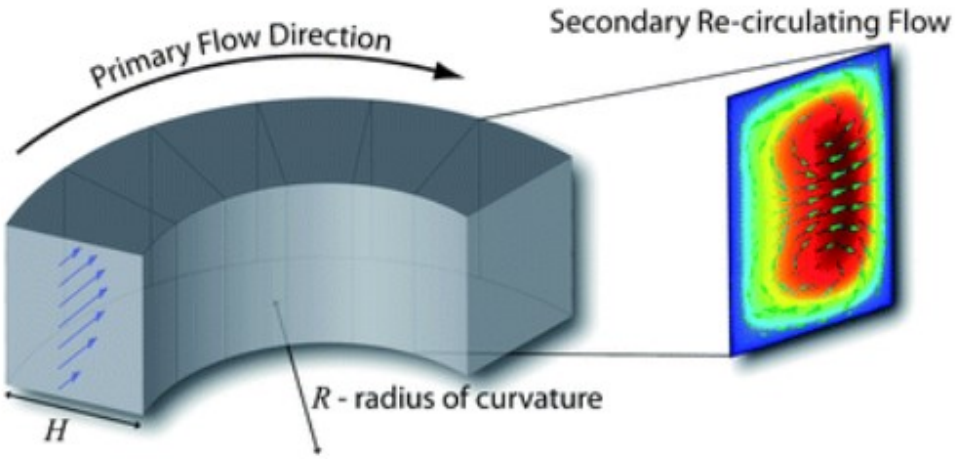

Figure 9 Curvature induced Dean secondary flows in an inertial separation device with design including curvature (24).

Typically, the Dean vortices are counter-rotating along the cross-section of the channel as seen in Figure 9 (14). Dean flow produces Dean drag force that balance with inertial lift force, thus providing flexibility to control equilibrium positions. Secondary Dean flow can help to reduce the equilibrium positions. Dean flow strength can be expressed as (20)

$$De = Re_c\sqrt{\frac{D_h}{2R}} \tag{8}$$

Where R is the radius of the curvature.

The Dean drag force is based on Stokes' drag law and is defined as (31)

$$F_D = 3\pi\mu d U_D \quad (9)$$

Where U_D is the transverse velocity defined as (31) (32)

$$U_D = 1.8 * 10^{-4} De^{1.63} \quad (10)$$

Dean drag force has linear size scaling whereas net inertial lift force has not (14). Thus concurrent effect is a result in distinct equilibrium positions of different sizes. Two empirical parameters have been determined for designing inertial focusing devices succesfully. First is the ratio between particle and hydraulic radius of the channel:

$$\frac{d}{D_h} > 0.07 \quad (11)$$

Second is the ratio between inertial lift force and Dean drag force

$$R_f = \frac{2d^2R}{D_h^3} \quad (12)$$

If the ratio is less than ~0.08, then inertial dominates over Dean force. Size-dependent differential focusing with the ratio of inertial lift force and secondary flow drag shows promise in an enhanced separation (20). However, too small leads to chaotic particle motion. Advantages of using a secondary flow channel are the application to range of different fluids of varying viscosities, densities and conductivities. However, at lower flow rates, the mixing becomes negligible.

Lin et al. (33) proposes that new equilibrium positions (Figure 10) can be estimated as

$$\frac{F_L}{F_D} \sim \frac{1}{\delta}\left(\frac{d}{D_h}\right)^3 {Re_c}^n \quad (13)$$

Where n < 0 and the curvature ratio is

$$\delta = \frac{D_h}{2R} \quad (14)$$

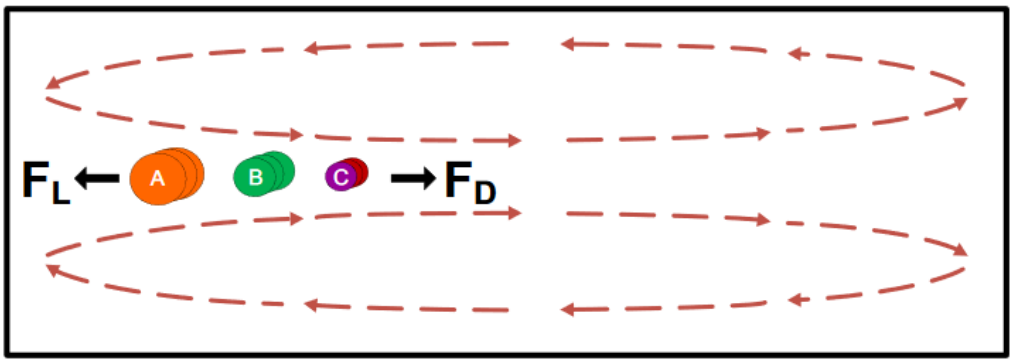

$$\left[\frac{F_L}{F_D}\right]_A > \left[\frac{F_L}{F_D}\right]_B > \left[\frac{F_L}{F_D}\right]_C$$

Figure 10 Particle size influences the equilibrium position as seen in cross-section of a microchannel with curvature. Equilibrium positions can be estimated as a ratio of lift forces over Dean drag force (30).

Deformability of cells influences the focusing in inertial microfluidics. Hur et al. (34) studied how deformability influences non-rigid particles. It is generated by shape changes of particles and nonlinearities at the interface of the particle surface due to matching of velocities and stresses. The direction is toward the centreline as seen in Figure 11. The change to equilibrium positions may be small, but there could be significant difference with rigid polystyrene particles and deformable cells (20). Also, the properties of the medium have impact on the inertial migration and equilibrium positions (2).

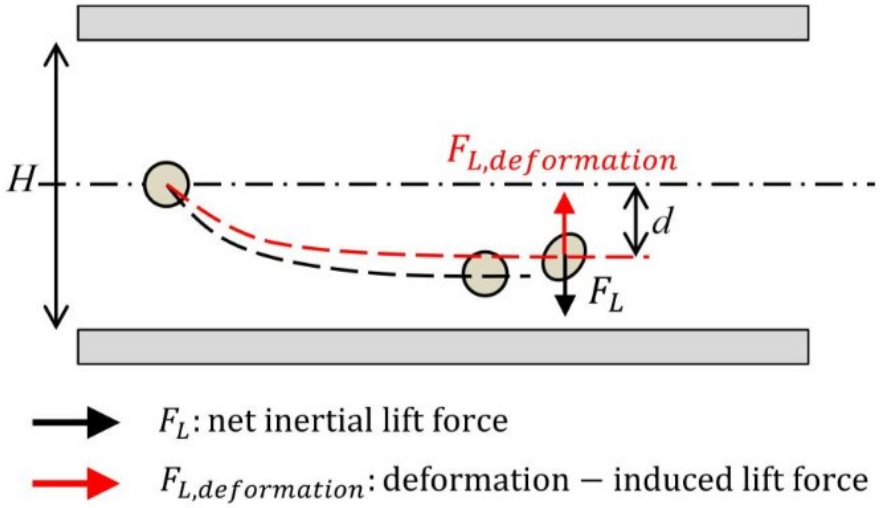

Figure 11 Particle deformation influences the equilibrium positions (2)

3.2 Channel geometries

Zhang et al (2) categorise inertial microfluidic devices by the channel structure as straight, spiral, straight channels with pillar arrays or expansion-contraction arrays and serpentine channels.

3.2.1 Straight channel

In a tubular channel the equilibrium positions are 0.6 times from axis as seen in Figure 6a (2). In a square channel, there are four equilibrium positions (Figure 6b), while in a low aspect ratio channel the positions are reduced to two (Figure 6c). In a straight channel there is a minimum length for sorting. Advantages of a straight channel is simplicity and ease of operation (2). Disadvantage is that lift force is proportional to inverse of channel hydrodynamic length, which cause limitations to channel cross-sections. Furthermore, the length of the device is moderately long, which builds the flow resistance and device footprint. Example is seen in Figure 13.

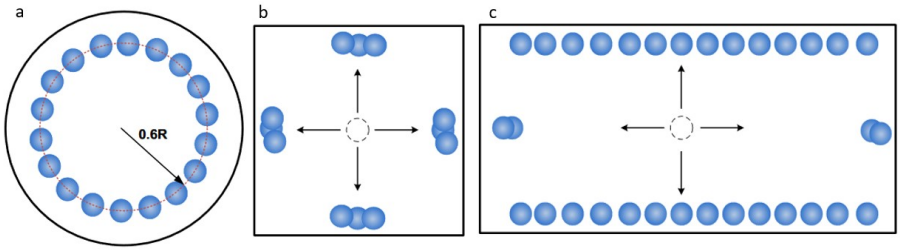

Figure 12 Equilibrium positions in straight channel cross-sectional views. a) a tubular channel, b) a square channel and c) rectangular channel. (30)

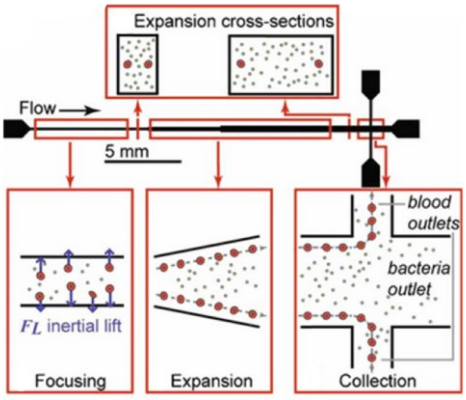

Figure 13 Straight inertial microfluidic channel that separates bacteria from blood by focusing larger blood cells to trajectories near wall. The smaller bacteria remain unfocused. (35)

3.2.2 Spiral channel

The spiral channel has a curvature along a single direction (2). The secondary flow is formed from the mismatch between the near-wall and centre area fluids. Near the centreline of the channel, the fluid elements have larger inertia from centrifugal effect, which causes pressure difference gradient in radial direction.

Zhou et al (36) proposes that the inertial lift forces lead particles to equilibrium positions and the Dean drag influences those positions by entraining the particles within the vortices. In a simple spiral, larger particles are attracted more closer to the inner wall. Dominating force is the net inertial lift, but the Dean flow speeds up the process of finding the equilibrium positions as well as reducing them (31).

Advantages are superior throughput, low clogging and excellent efficiency and purity has been proven (31). Disadvantages are a large footprint for a microfluidic chip and rigid geometry that can not be changed for other sizes.

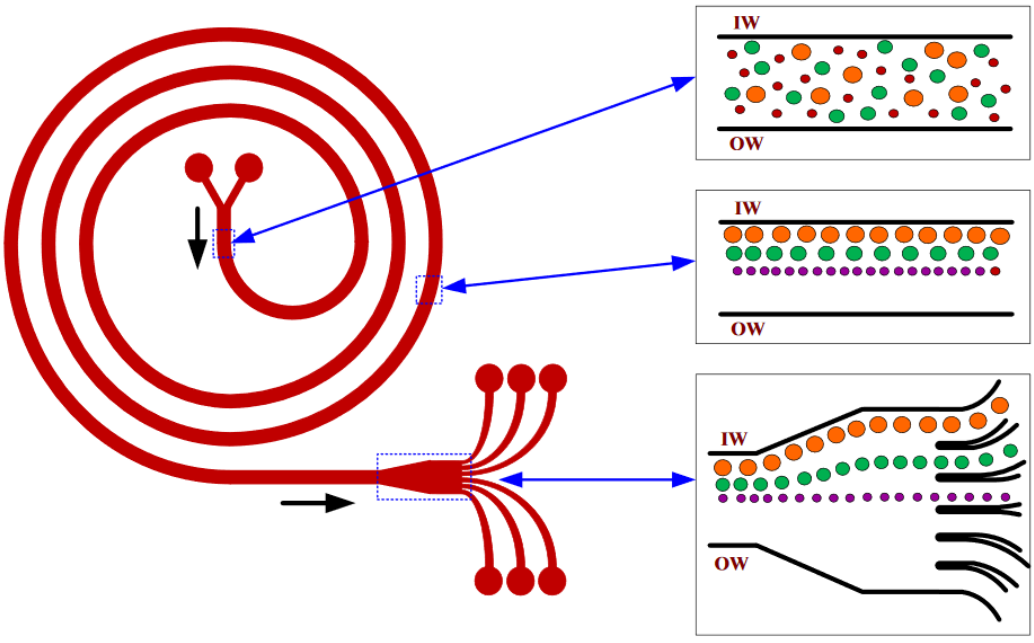

Figure 14 Spiral type separation microchannel. Larger particles migrate toward inner wall (IW) and smaller particles toward the channel centre. (30)

3.2.3 Serpentine channel

Serpentine channel has alternating curvatures that may not have enough time for the secondary flow to reach steady state unlike in spiral structure (2). In a serpentine system the number of equilibrium positions may be reduced, and the particle are rather focused than separated. The ratio between forces is relating to particle diameter and channel dimensions. Larger particles are fast to focus, whereas smaller may remain unfocused, if the Dean drag force is too large. The major drawback of this is that the geometry needs to be designed with a distinct particle size in mind. Focusing can occur in three types, two-sided focusing, transitional focusing and single central focusing. High throughput is though a major advantage of serpentine channel even thought the design needs to be long to get all particles to a steady state of focusing.

Zhou et al (14) used serpentine asymmetric design of series of reverse wavy channel structure to focus and sort out particles and cells by size as shown in Figure 15. They promised of 89.72 % recovery for MCF-7 cells and enrichment from original purity of 5.3 % to final purity 68.9% with excellent viability.

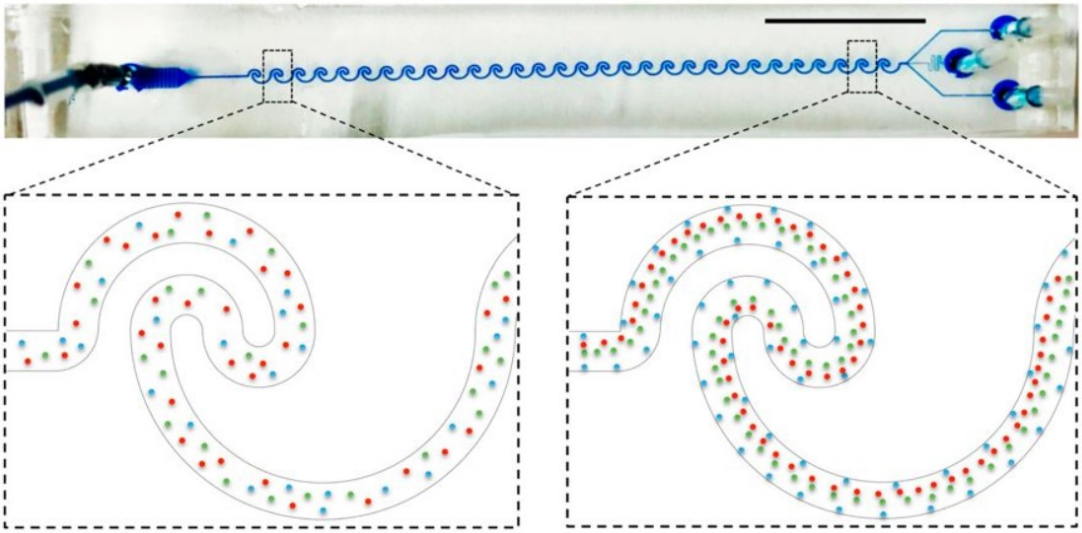

Figure 15 A serpentine type microfluidic channel 10 µm (red) and 15 µm (green) particles focus to single streams near centre, while smaller particles such as 3 µm particles (blue) focus in double streams near walls (14).

3.2.4 Contracting-expanding channels

Consequence of series of alternating narrow (contracting) and wide (expanding) geometries, is a unique vortex formation under low Re_c at the corners of expansion channel (20). Vortexes in an orifice channel are different to Dean vortexes in curved channel, or in an asymmetrical channel. Vortex formation relies on ratio between contracting and expanding channel cross-sections, angle and roundness of the orifice corner, surface roughness and fluid inertia. High Reynolds number results in turbulence around the particles, while low Reynolds number reduce particles passing through the contracted area. Single line of focusing can occur with moderate Reynolds, appropriate channel aspect ratio and volume fraction. At the entrance of contraction region, centrifugal forces induce counter-rotating secondary flow and the sample flow is enveloped with three dimensions (2). The larger particles or cells are moved by dominantly inertial lift towards the contraction-expansion side of the channel, while the smaller particles are coverned dominantly by Dean drag and remain on near the channel wall opposite to the expansion side. Additionally, the channel can have orifices on both sides, which is termed as Multi-orifice flow fractionation, MOFF. Advantages are continuous, label-free, sheathless, non-intrusive, but the recovery may remain low. Example of a MOFF device is shown in Figure 16.

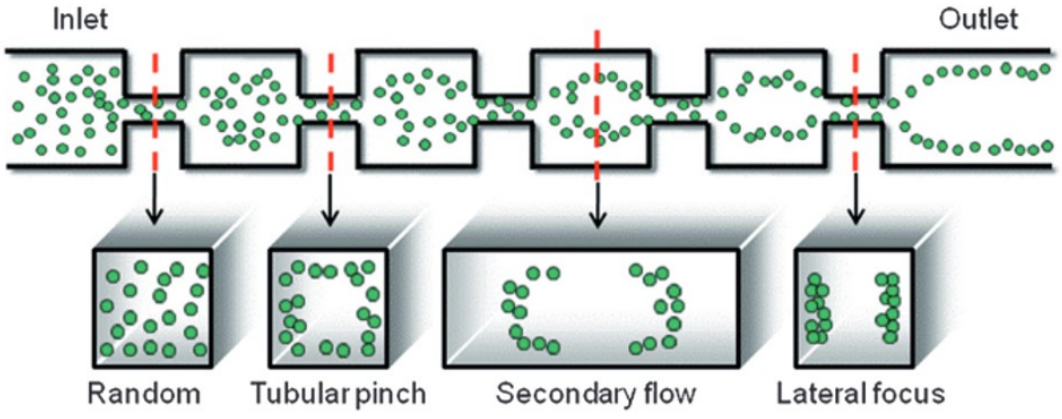

Figure 16 In an expansion-contraction type of microfluidic channel the particles experience alternating tubular pinch in contraction regions and Dean secondary flow in expansion regions (37). At the end, particles are laterally focused near the wall; smaller particles closest to wall and larger closest to centre.

3.3 Spiral Chip

Shen et al (31) demonstrated with micro-obstacles in spiral design the enhanced effect of particle separation by inertial forces and Dean secondary flow that is enhanced by micro-obstacles confinement (Figure 17). They were able to separate 7.3 µm, 9.9 µm and 15.5 µm particles with the largest size flowing to inner outlet. Shen et al. (31) promise high throughput (over 22000 particles/s) and long-duration operation (at least 4 h).

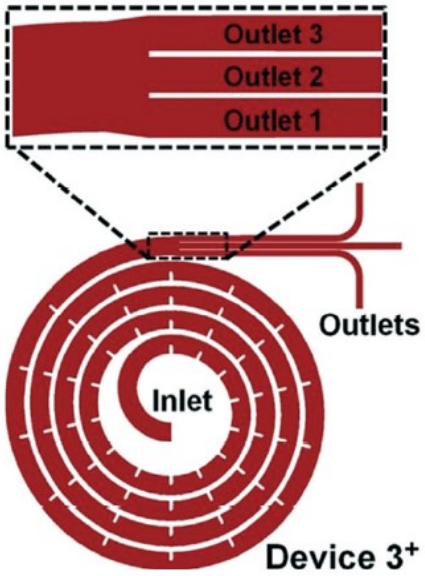

Figure 17 Spiral chip design utilizes inertial lift and secondary flow as well as expansion-contraction type separation induced by ridges (31).

Shen et al. (31) designed the chip to have a very low aspect ratio to achieve high throughput. They also speculated that the decrease in the curvature radius, when the flow encounters the micro-obstacle is significant to the acceleration of the secondary flow. They promise an easy-to-use, effective, high-throughput, continuous and sheathless particle manipulation device. Particle are effectively focused up to 99.8 %, collected up to 98.7 % and with 98.4 % purity. Cell lines the efficiency was 97.5 % for MCF-7 and for 92.3 % HeLa. Additionally, viability and growth were not affected. They demonstrated effective CTCs separation and collection using 6.5 ml/min flow rate with diluted whole blood with $1{:}10^7$ CTC-to-blood ratio and they achieved to get $1.89{\cdot}10^9$ cells per min throughput, with >97% collection efficiency and over $2.29{\cdot}10^5$ -fold enrichment.

3.4 Labyrinth Chip

Labyrinth chip is the term designated by Lin et al. (33) (38) for a serpentine type inertial microfluidic chip (Figure 18). It uses alternating curvatures to induce both net inertial forces and Dean vortices to separate cells. Additionally, the sharp corners in the design are expected to mix especially the smaller particles to migrate them more efficiently toward the equilibrium positions. Microfluidic mixing with a zigzag type channel with sharp corners is found to mix solutions effectively (39). The design has a large footprint (device diameter over 5 cm). However, Lin et al (33) (38) were able to separate successfully various cell lines of CTCs successfully with >90 %. Operating flow rates range from 0.5 ml/min to 3 ml/min with optimal flow rate of 2.5 ml/min using CTCs from whole blood. Promises to separate CTCs (15-25 µm) from blood cells (2-12 µm). The labyrinth offers high throughput, preserves cell viability and has the potential for downstream analysis. Lin calculated that due to the size difference of WBCs and CTCs, the length of the separation channel required is different. To achieve high recovery and to prevent carryover of both, the channel should be designed for both. In Lin's (33) calculations the CTCs would require at least 480 mm channel to focus. The final design was 637 mm in lenght, 500 µm width and ~100 µm height (Figure 18).

Figure 18 Labyrinth chip design first balances the net inertial lift forces, then the Dean secondary forces induced by alternating curvature and finally, the focusing is enhanced by mixing effect of the corners (33).

3.5 Concentrator Chip

Microfluidic processing of bioparticles may result in solutions of high volumes with low volume fractions. Thus, concentration of processed solutions is beneficial for example to produce less fluid to image, when analysing with microscopy. The concentrator chip designed by Martel et al (40) is based on combination of inertial focusing and siphoning. Their chip consists an initial inertial focusing zone after which it separates into combination of focusing and siphoning channels as seen in Figure 19. In their design they promise 95 % yield with 240 ml/hour throughput with a design that consists ten parallelized 10x concentrators in series with 50x concentrator.

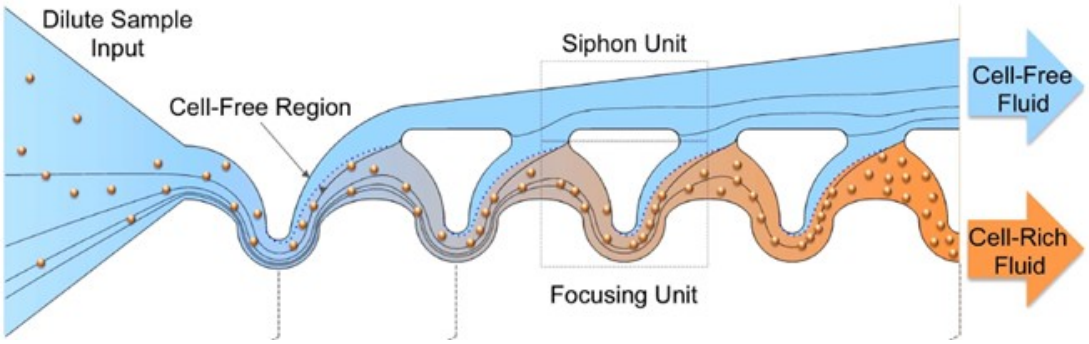

Figure 19 Concentrator chip first focuses the particles in a focused streamline from dilute sample (40). Then the channel spreads to focusing and siphoning channels, in which the focused particles continue along to the focusing channel and excess fluid siphons to siphoning channel.

Focusing units are designed to induce focusing for above 8.5 µm cells such as WBCs from diluted blood. The amount of siphoned fluid from the cell free region at the focusing unit is dependent on the hydraulic resistance of both channels. Higher siphoning may cause particles to siphon as well, if the inertial forces are not enough to keep particles within the equilibrium positions of the flow. Martel et al (40) optimized their designs evaluating with various focusing channel widths and 75 µm was found optimal. They used 9.9 µm fluorescent beads in 10^6 particles per ml. Optimal flow rate was determined to be 500 µl/min. They obtained yield over 95 %, when device was operated within 400 to 600 µl/min range both with particles and WBCs.

3.6 Non-Equilibrium Inertial Separation chip

Non-Equilibrium Inertial Separation chip (NISA chip) combines inertial forces and siphoning to separate WBCs from whole blood. Mutlu et al. (18) obtained with a 104 parallelized design high throughput 400 ml/h of whole blood with 96.6 % WBC yield with only 0.0059 % RBC carryover using 1:1 diluted blood. The ratio of blood and buffer flow rates were 1:40. Inertial forces in the chip are induced by the wall, which repels particles deterministically. The larger particles follow main channel, but the smaller particles are siphoned to other trajectories due to pressure difference induced from the array geometry (Figure 20). The trajectory difference is due to strong correlation between lift force and particle size i.e. $F_L \sim a^6$. According to Mutlu et al. the particles do not achieve equilibrium positions and inertial wall lift is adeaquate, which leads toa compact design. One channel device was designed to have an array of n (rows) x m (columns) with siphon percentage (τ) calculated from the hydraulic resistance difference. They used 7 µm as threshold cell size. Optimal results were gained, when flow rate of 80 µl/min per row was used. Optimal compromise was gained with siphon percentage 3.6 %, in which Mutlu et al. (18) achieved 92.1 % WBC yield and 0.0036 RBC carryover.

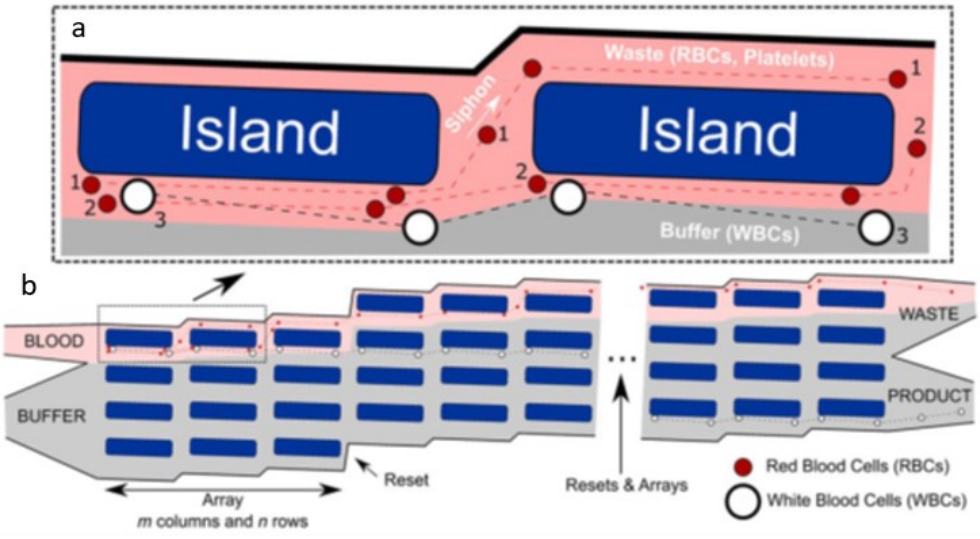

Figure 20 Trajectories of small red blood cells and large white blood cells are different due to wall induced lift force. The smaller particles continue along next to the island wall and siphon to waste outlet and larger particles continue along the main channel to product outlet. a) the particle trajectories near islands. b) conceptual design of the NISA device particles (18).

3.7 Comparison of chip details

We have discussed the peer reviewed articles of Spiral, Labyrinth, Concentrator and NISA chips. The relevant features of the devices are summarized in Table 1.

Table 1 The combination of essential facts of the devices.

Device	**Spiral chip** (31)	**Labyrinth chip** (33) (38)	**Concentrator chip** (40)	**NISA chip** (18)
Material	PDMS	PDMS	PDMS	COP or PDMS
Physics or mechanism	Inertial lift and secondary flow	Inertial lift, secondary flow and corner mixing	Inertial focusing and fluid siphoning	Wall induced inertial lift and siphoning
Flow rate range	Up to 10 ml/min	Up to 3 ml/min	Up to 0.6 ml/min	1/40 ratio: feed to buffer (up to 0.4 ml/min)
Optimal flow rate	6.5 ml/min for cells	2.5 ml/min	0.5 ml/min	80 µl/min between the islands
Particles [µm]	7.3, 9.9, 15.5 PS	-	10 PS fluorescent	5, 7 and 10 PS fluorescent
Cells	HeLa, MCF-7, K562 and whole blood	Various cell lines of CTCs	WBCs	WBCs from blood
Throughput	$1.89 \cdot 10^9$ cells/min	2.5 ml/min	4 ml/min	3 ml/min, $300 \cdot 10^6$ cells/min
Efficiency, yield	>97% efficiency of CTCs from diluted blood	>90 % of efficiency with various cell lines	95 % WBC yield	97 % WBC yield

4 Materials and Methods

In this chapter, we describe the materials, methods and device designs that were used for device fabrication, microfluidic assembly and operation, and finally what characterization methods were used for particle and cell separation.

4.1 Device Fabrication

Microfluidic devices were fabricated using soft-lithography, where SU-8 master is used for pattern transfer on PDMS. Then, the channels are sealed with bonding PDMS on microscopic slides and assembling the device to a syringe pump with tubings for flow rate testing.

4.1.1 SU-8 Master

SU-8 master was fabricated with UV-lithography using negative photoresist SU-8 on a 100 mm silicon wafer. First, the wafer was cleaned of native oxide with dipping into buffered Hydrofluoric acid for ~15 s, rinsing with DIW and heating in 250 °C. SU-8-50 (MicroChem) was then spun on the wafer with BLE spinner tool ramping up to final spin of 1300 rpm for 30 s. Then, the SU-8 was soft baked on hotplates for 900 s in 65°C and 900 s in 95 °C ending to at least 15 min cooling period. Next, the wafers were exposed to UV through a photomask to transfer the pattern with exposure time 25 s using 365 nm. The masks used in the project were designed during autumn 2017 for “Group Research Assignment” -course in Aalto university, the School of Chemical Engineering. The post exposure baking was done to crosslink the polymer on UV exposed areas on hotplates in 95 °C for 600 s. Then, the wafers were developed (MR-DEV-600, micro resist technology, for 15 min with IPA and drying), in which the unexposed areas were dissolved in the developer. Afterwards, the depth measurements were done with a profilometer Bruker DektakXT. Additionally, SU-8 side of the wafers was coated with a fluoropolymer antiadhesion coating using RIE Oxford PlasmaLab 80 Plus for ~8.5 min in CF_4.

4.1.2 PDMS

Sylgard 184 PDMS (Dow Corning) was used in 10:1 ratio of monomer and curing agent. After mixing, the PDMS was degassed for 30 min. Then, PDMS was poured on SU-8 master and cured at 65 °C for 2 hours. The PDMS was peeled from the master and the devices were cut to fit 2´x3´ microscope glasses. Outlets/Inlets were punched with a 1.5 mm puncher. Other punchers tested were 1, 2 and 3 mm.

4.1.3 Bonding PDMS to glass

First, surfaces were cleaned for effective bonding. Cleaning of chips was done with 30:1 PDMS or with adhesive tape after cutting and punching. Cleaning of microscope slides was done first with clean room paper and acetone, and then with IPA and drying. After cleaning, both PDMS and glass were treated with oxygen plasma using TePla 400 (PVA TEPLA) with recipe of 60 W and 500 ml/min of O_2 for 1 min. After plasma treatment and pressing surfaces together, the bonded device was baked in 15 min 65 °C. Figure 21 shows the Spiral, Labyrinth and Concentrator chip in comparison to a 50 cent coin, when bonded successfully on microscope slide.

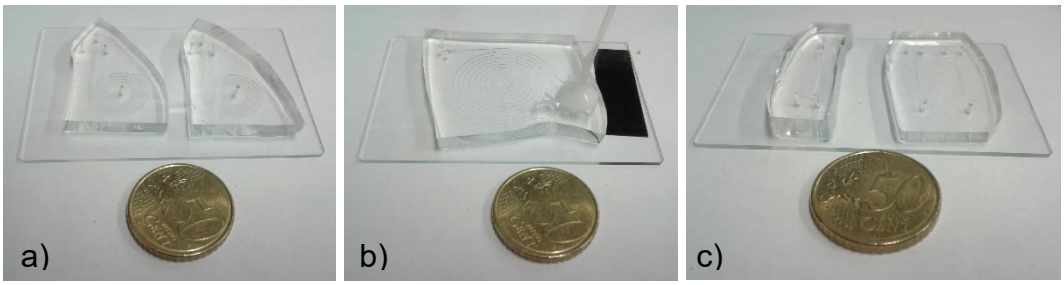

Figure 21 Spiral chips (a), Labyrinth chip (b) and Concentrator chips (c) imaged after bonding.

4.2 Fabricated chips

Here are the fabricated chips reproduced from the main articles described in chapter 3. The channel height of NISA and concentrator chip are ~52 µm and Spiral chip and Labyrinth chip are ~100 µm. Height error is ± 2 µm. The article heights are 52 µm for NISA chip and Concentrator chip, and around 100 µm for both Spiral chip and Labyrinth Chip.

4.2.1 NISA

The reproduced design is according to article design (18). The uppermost siphoning channel width is 20 µm, island length is 200 µm and island width 50 µm. Dimensions used for calculations consists of length 55 mm, height 52 µm, main channel width 350 µm and width between islands 20 µm, 50 µm, 50 µm and 80 µm. There was other two designs altering the NISA article design. The other two designs were otherwise same except for the uppermost siphoning channel, island length and the changes that they induced gradual on the array. First different design had 20 µm uppermost siphoning channel width and island length of 150 µm. The second had 12 µm uppermost siphoning channel and island length of 200 µm. The two were tested preliminary with DIW and particle solutions. The design seen in Figure 22 was chosen to be experimented with and was also the one resembling the article design to gain more comparable results. Figure 23 shows an optical microscopy image of the array shift. The islands are seen clear trenches in SU-8 pattern.

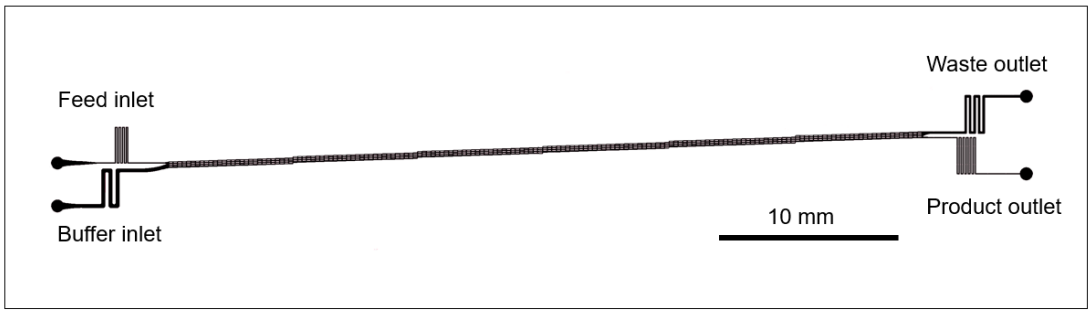

Figure 22 The NISA chip mask. Design with island length 200 µm and width 50 µm, array size 3 x 28 islands, channel size 6 x arrays.

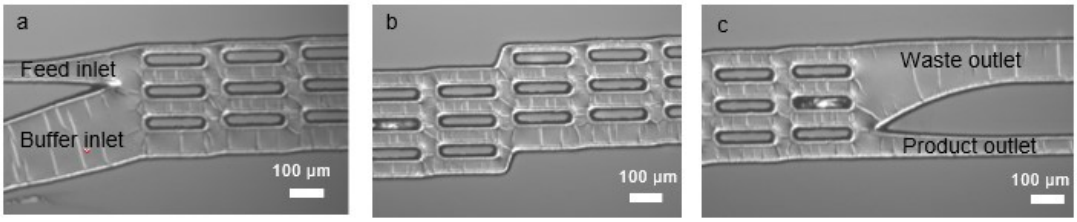

Figure 23 SU-8 Master brightfield 5x optical microscopic images of NISA chip show inlets (a), array shift (b) and outlets (c). The array shifts upward after 28 islands, which shifts the particles so that the smaller red blood cells continue upward and toward waste outlet and larger particles continue toward product on main channel.

4.2.2 Spiral chip

The replicated design seen in Figure 24 from the article (31) has different seven outlets instead of three used (Figure 25b and c). Otherwise the design is similar; the ridges are the same size as in article, 200 µm x 450 µm (Figure 25a). Dimensions used for calculations are length 160 mm, height 100 µm, the main channel 900 µm and ridge length 450 µm. There was another design of alternating spirality, the other run clockwise and the other anti-clockwise. Both were tested preliminarily with DIW and particle solutions.

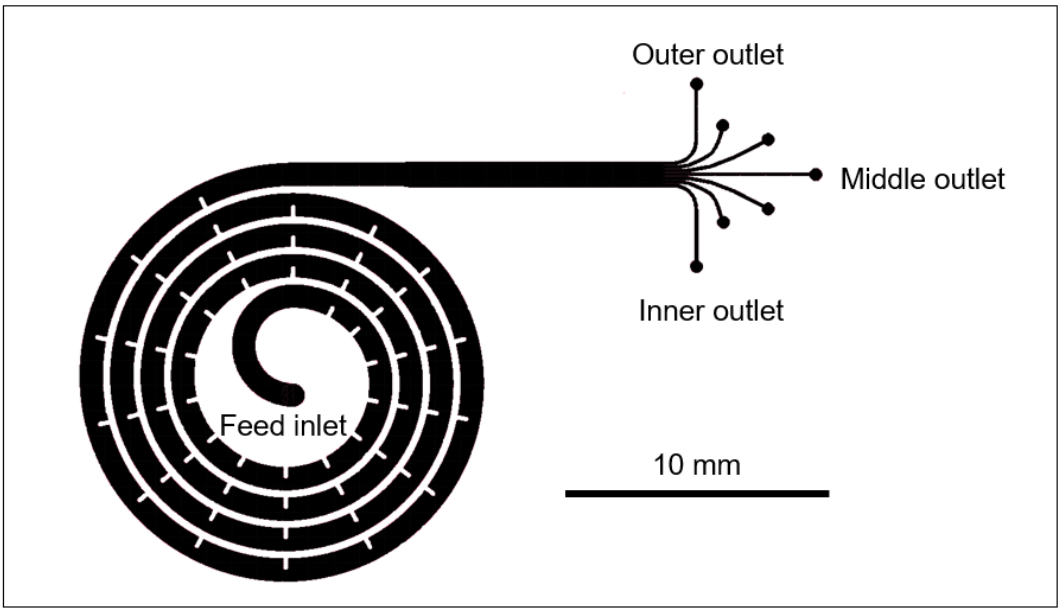

Figure 24 The spiral chip mask. Design consists seven outlets, but only Outer, Middle and Inner outlets are opened.

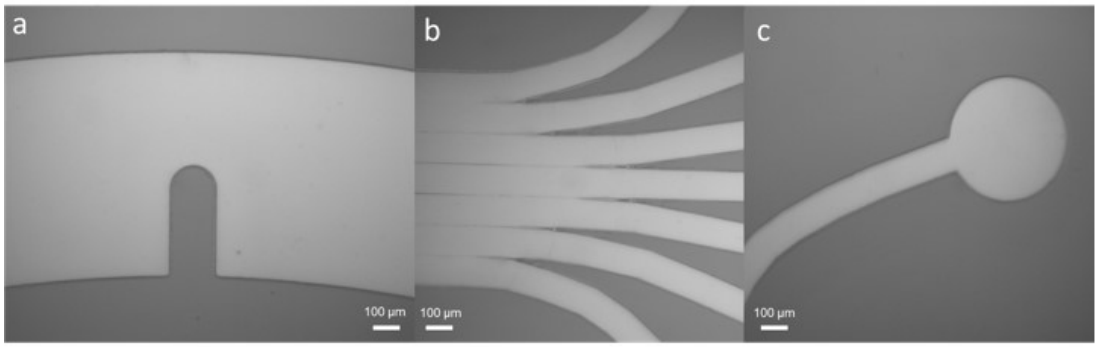

Figure 25 Optical microscopic brightfield 5x images from Spiral chip bonded. The ridges (a) are half the length of the main channel width. There is seven outlets (b) in our design, but only three are opened. The outlet channel ends in wider circle (c) to fit the tubing.

4.2.3 Labyrinth chip

The reproduced design seen in Figure 26 is according to article design (33). Dimensions used for calculations consist length 835 mm, height 100 µm, main channel width 500 µm. There was a ridged version designed and two versions with article outlets and one with seven outlet design. The designs were tested preliminarily with DIW and article version was chosen for the comparable data reasons. Figure 27 shows optical microscopic images of corner and outlet details from Labyrinth chip.

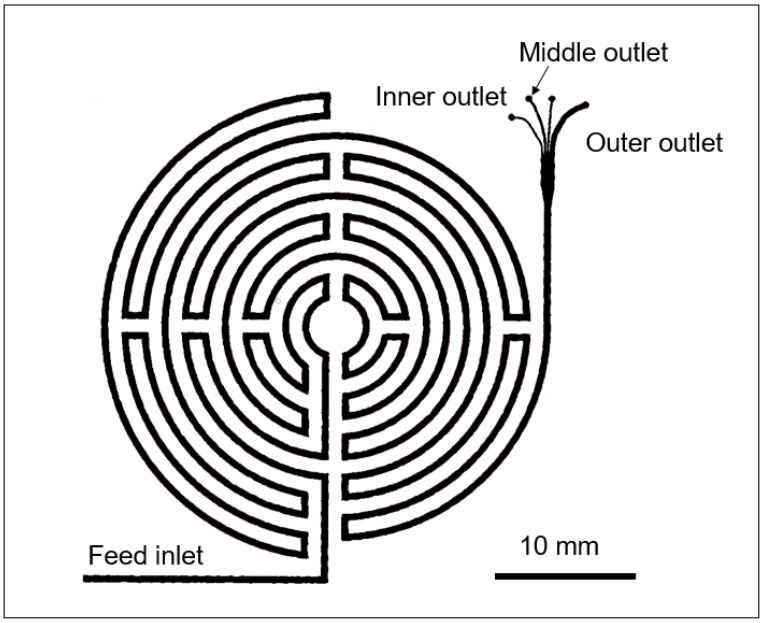

Figure 26 The Labyrinth chip mask. Design consists four outlets, but only inner, middle and outer are opened.

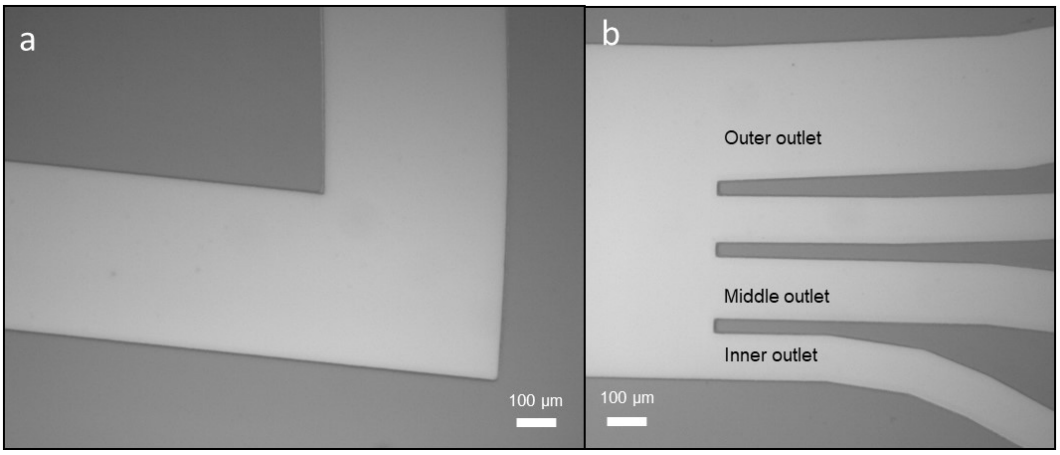

Figure 27 Labyrinth chip has sharp corners (a) and four outlets (b) of which the named ones are opened due to tubing space restrictions. Optical microscopic images taken with 5x brightfield.

4.2.4 Concentrator chip

The replicated design seen in Figure 28 is according to article design (40). Dimensions used for calculations are length 30 mm, height 52 µm, width of the focusing channel 75 µm, siphoning channel near inlet width 28 µm and near outlet width 260 µm. There was a design version that had both focusing channel and siphoning channel changing gradual towards the outlets and the other version with only siphoning channel widening gradually towards the outlets. The article version was chosen for the purposes of concentration, but also because preliminary particle testing resulted better concentration in the article version. Figure 29 shows the detail of how the focusing channel spreads to continuation of focusing channel and siphoning channel and the detail of how the siphoning channel grows until waste outlet and focusing channel leads the particles on focused stream toward product.

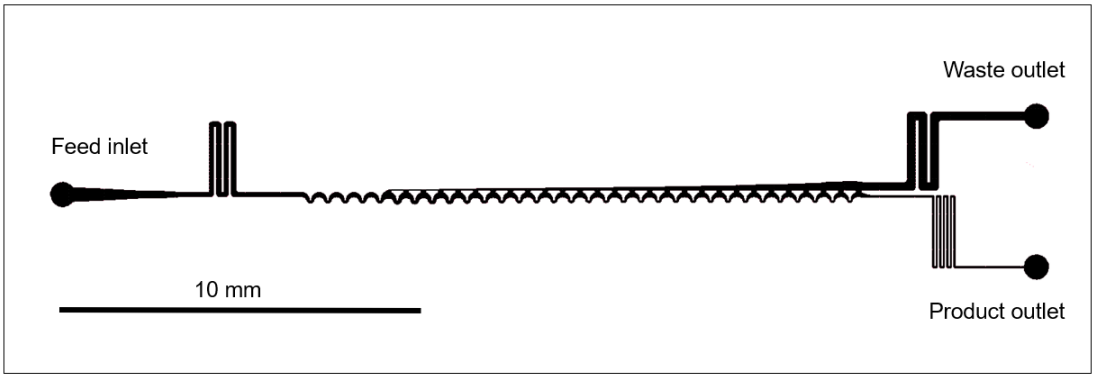

Figure 28 The concentrator ship mask

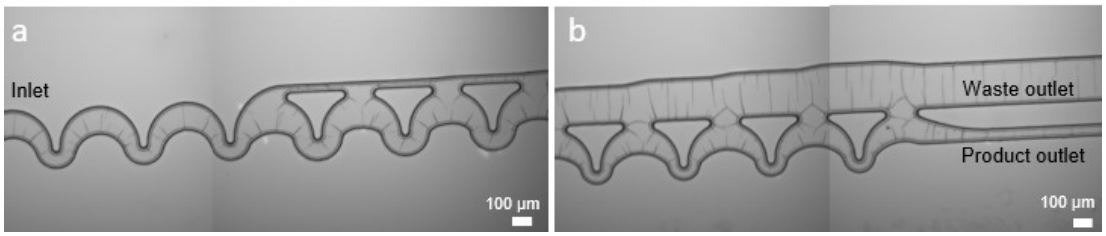

Figure 29 Concentrator chip starts with a focusing channel (a) that spreads into focusing and siphoning channels. The focusing channel dimensions remain the same while the siphoning channel widens toward the waste outlet (b) due to hydraulic pressure difference. Master imaged with 5x brightfield.

4.3 Device operation

The experimental setup (Figure 30) consists syringe pump (Aladdin Single-Syringe Pump AL-300), syringes, connectors and glass vials. NISA chip was tested with two syringe pumps. Syringes were either slip or luer lock lock from 1 ml to 60 ml from several different suppliers. The most used syringe was sterile 20 ml slip lock syringe from BD. Connectors included needles, luer locks and tubing. Needles from 17” to 19” gauge were used. Needles were tested without cutting the tip and with the tip cut, rounded and smoothened to prevent holes, when connecting it to the tubing. The tested tubing was silicone or Teflon from 1/32” to several millimetres. 1 cm of Teflon 1/32” tubing was fitted up to ¾ inside 1/32” silicone tubes (50 cm for inlet and 10 cm for outlets) and then it was fitted to inlets and outlets of 1.5 mm punched holes. Then, the silicone tubing was pulled on top of the needle, which was fitted to syringe with luer slip. The syringe pump and several vials are shown in Figure 31. In high pressure devices, Labyrinth and NISA chips, the needle was glued to tubing from top and the inlets were glued from top after inserting the tubing tightly to inlet. Figure 32 has four Concentrator chips bonded to glass, and one connected with tubing.

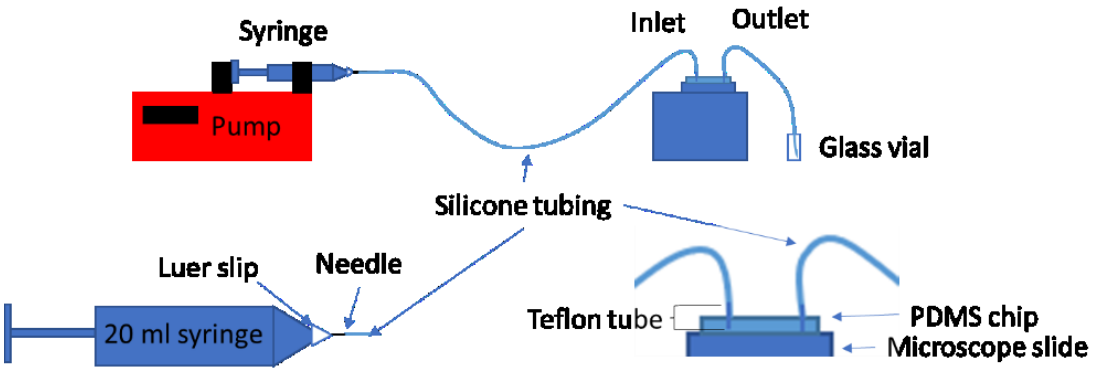

Figure 30 Experimental setup for flow rate tests and details of syringe and tubings.

Figure 31 Syringe pump in the background is pumping 2,5 ml/min to assembled Labyrinth chip during cell medium test. Sample is gathered to vials; outer, middle and inner outlets.

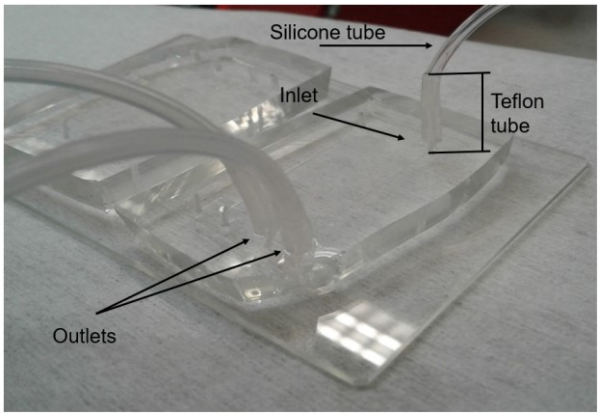

Figure 32 One concentrator chip is assembled with connectors using Teflon and silicone tubing. Device has one inlet and two outlets.

4.4 Particle and Cell Samples

Particles used for tests were 8, 10 and 15 µm PS microparticles (10 % solids) from Sigma-Aldritch. Particle solutions were diluted with DIW, which was also used to test initially the flow rates, pressures and leaking.

Additional chemicals used in experiments were low Mw salt, surfactants and solvents. Table salt was added 1 to 5 wt-% to test particle sedimentation. SDS (1 %) and Triton-x (1 %) were tested with 8 µm and 10 µm in NISA chip. Solvents DIW, acetone and IPA, were used during the experiments.

Preliminary tests were also done with cells in medium and PBS. Perkin Elmer provided placental JEG-3 (ATCC® HTB-36™) cells from in vitro cultures. Concentrations were 100k, 50k, 10k cells in ml in cell medium or PBS. Medium used was Eagle's Minimum Essential Medium, (EMEM ATCC® 30-2003™). Cells were disposed using Virkon S from Du Pont.

4.5 Particle Measurements

Microparticle feed and outlet sample solutions were tested with Laser Diffraction and Optical Microscopy. Microparticle physiochemical properties have been characterized with electron microscopy (SEM, TEM), dynamic light scattering, zeta-potential measurement, X-ray photoelectron spectroscopy, atomic force microscopy, optical light and fluorescence microscopy (41).

Efficiency of cell separation can be defined with recovery, purity, collection efficiency and enrichment (14) (42). We estimated our microparticle results with literature definitions:

$$\text{Recovery} = \frac{\text{Number of target cells in each output}}{\text{Number of target cells in input}} \quad (15)$$

$$\text{Purity} = \frac{\text{Number of target cells in each output}}{\text{Total number of cells in each output}} * 100\% \quad (16)$$

$$\text{Collection efficiency} = \text{Recovery} * 100\% \quad (17)$$

$$\text{Enrichment} = \frac{R_{outlet1}}{R_{inlet}} = \frac{\frac{Target\ cells\ in\ outlet\ 1}{Other\ cells\ in\ outlet\ 1}}{\frac{Target\ cells\ in\ inlet}{Other\ cells\ in\ inlet}} \quad (18)$$

4.5.1 Laser Diffraction Particle Measurements

Laser Diffraction measurements were performed with Malvern Mastersizer 2000 and Hydro 2000 MU. Method is used for samples of wet dispersion to detect particle sizes within range of 0.1 -1000 µm (43). It is a non-destructive analysis of wet and dry samples. Mie theory and reflective index of 1.59 for PS was used. Mastersizer determines from the captured optical data the scattering patterns of particles and calculates the distribution for particle sizes. Measurement was done in following way. 400 ml beaker was placed with DIW level over the stirrer (43). Then, the pump was started, 1500 rpm. First, the baseline for DIW was determined. Then sample is placed in the 400 ml beaker, when circulation is off. The beaker is ultrasonicated for 10 s and the pump is started again. Now sample is flowing through the system and particles are passing through the analyser light in optical cell. Obscuration of light done by particles is recommended to between 10-20 %. In the optical bench the scattering pattern is captured by the detector array.

4.5.2 Optical Microscopy

The Zeiss Opton optical microscope was used for imaging. µEye cockpit -software was used together with EO-10012M Edmund 3 fps monochrome camera. Brightfield was used for imaging devices, cell sample solutions and videos. During videos the devices were set-up with 3D printed stage attached to the microscopic stage with tape (Figure 33).

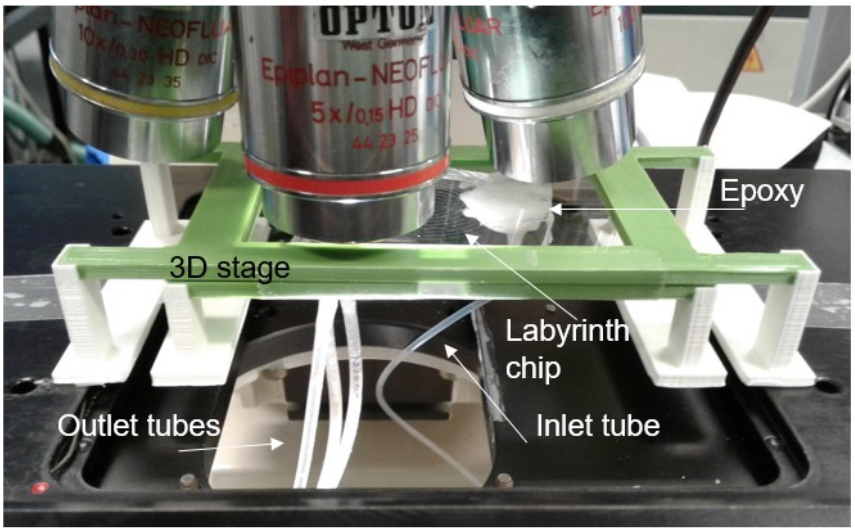

Figure 33 Labyrinth chip attached to 3D printed stage. Three soft silicone tubing seen in the image are taped together to a liquid collection vial. Samples are not collected during videos.

We evaluated different methods to gain processable images of the particles in a droplet on and between glass sides, on different grids and dark versus brightfield modes. Used method consists; a droplet of 3 µl was inserted between two thin 20 mm x 20 mm microscope slides and on top of a 3x3 (10 mm x 10 mm) transparency grid. Middle point of the droplet was put on top of the middle screen in the grid. Microparticle samples were imaged with our developed nine image counting method in dark field mode of 5x magnification from all nine screens of the grid. Each sample was repeated thrice. Example image can be found in Appendix A. Then the images were processed with ImageJ2 (44) and image processing package Fiji (45). Processed image and Coremacro for image analysis can be found in Appendix A. The number of images (four, five or nine) used for the experiments was evaluated statistically and the error of using nine images was less than 15 %. Average counts of particles can be found in Appendix B and average cell counts in Appendix C.

5 Results and Discussion

In this chapter, the experiments to characterize the chip operations are described. First, the results on experiments with each device are examined. Then, some general issues that apply to all devices are discussed. Finally, comparison of microparticle and cell experiments are discussed.

Flow rates and solutions were selected to reproduce the data of articles by Lin et al. (38) (33), Martel et al. (40), Mutlu et al. (18) and Shen et al. (31). The series of experiments were designed to use baseline flow rate from the articles and ± 30 % of baseline flow rate, shown in Table 2. NISA chip flow rates were chosen by estimations to fulfil a baseline flow rate (80 µl/min) between the islands.

Table 2 Particle test parameters

			Flow rates [ml/min]		
Test series	**Feed, PS particles in DIW**	**Tests**	**- 30 %**	**Baseline**	**+ 30%**
Concentrator chip	0.1 M 10 µm	3	0.35	0.5	0.65
Spiral chip	1M 1:1 10 µm and 15 µm	3	4.9	7	9.1
Labyrinth chip	0.1M 1:1 10 µm and 15 µm	3	1.75	2.5	3.25
NISA chip	1M 1:1 8 µm and 10 µm	1	0.006	0.008	0.01
	Buffer fluid DIW		0.23	0.31	0.4

Additionally, cells were investigated with Concentrator chip, Spiral chip and Labyrinth chip using the same flow rates as for particles with 10^3 to 10^5 cells per ml both in EMEM and PBS solutions.

The hydraulic resistance and pressure drop of the devices were calculated by using equation $\Delta P = R_h Q$, where $R_h = (12\mu L)/(wh^3 * \left(1 - \frac{0.63h}{w}\right))$ for rectangular channel seen in Table 3. Rough estimation shows that over 9 bar device and flow rate the epoxy gluing becomes advisable.

Table 3 Estimations of hydraulic resistances and pressure drop using straight channel with rectangular cross-section. Dimensions are given in experimental section 4.2 under each device.

Device	Flow rate [ml/min]	Hydraulic resistance [Pa/(m³/s)]	Pressure drop [bar]
Labyrinth chip	1.75	2.15E+13	23
See 4.2.3	2.5	2.15E+13	32
	3.25	2.15E+13	42
Without epoxy	3.0	2.15E+13	39
Spiral chip	4.9	2.50E+11	0.7
See 4.2.2	7.0	2.50E+11	1.1
	9.1	2.50E+11	1.4
Concentrator chip	0.35	2.84E+13	6.0
See 4.2.4	0.5	2.84E+13	8.5
	0.65	2.84E+13	11
NISA See 4.2.1	0.01/0.4	4.17E+13	10

The calculated results of the channel and particle Reynolds number (equation 3 and 5) for each experimented device is shown in Table 4. The estimations are done using the cross-section of main channel (Spiral and Labyrinth), between islands (NISA chip) or the focusing channel (concentrator chip) and the characteristic diameter is calculated from equation 4. Inertial forces are dominating over viscous forces in each device.

Table 4 The estimated Reynolds numbers for the experimented devices. Dimensions are given in experimental section 4.2 under each device.

Device	Optimal flow rate [ml/min]	Channel Reynolds number	Characteristic diameter [µm]	Particle Reynolds number		
				8 µm	10 µm	15 µm
Labyrinth chip See 4.2.3	2.5	255	83	2	4	8
Spiral chip See 4.2.2	7	460	97	3	5	11
Concentrator chip See 4.2.4	0.5	235	30	17	26	59
NISA chip See 4.2.1	0.08	47	25	5	8	17

5.1 NISA chip

We replicated the NISA chip design from Mutlu et al (18) using an array 3 x 28 of islands multiplied six times within one channel. It was investigated with feed solution of 8 µm and 10 µm 1:1 solution of 10^6 particles per ml and buffer solution of DIW. The flow rate ratio between feed and buffer was 1 to 40. The aim was to achieve flow rates in vicinity of the Mutlu et al's reported optimal flow rate of 80 µl/min between islands. Thus, the calculated flow rates were 0.008 ml/min for feed and 0.31 ml/min for buffer.

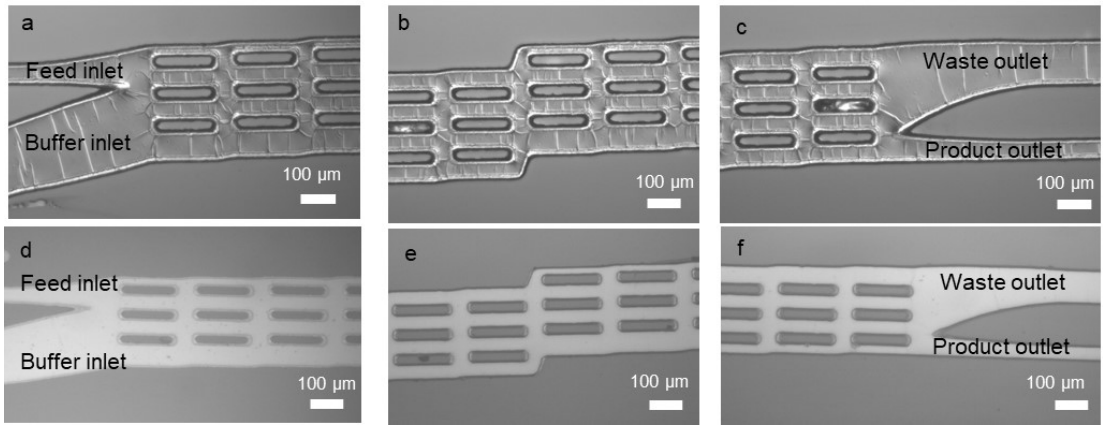

Figure 34 NISA chip master (upper row) and bonded chip (lower row) imaged with bright-field 5x. Master (a, b and c) has partially developed of SU-8 trenches as well as cracking. Bonded and glued device (d, e and f) images show that islands are fully bonded in air-filled channels. d) has been taken through thick microscope slide due to epoxy gluing, while e) and f) are taken through PDMS.

First, fabrication of NISA chip had issues in SU-8 development due to small features, i.e. trenches. This was seen in microscopic images (Figure 34) and resulted in insufficient bonding between PDMS islands and the glass, even when weight (from ~25 g up to ~330 g) was used on top during baking after bonding. The issue was resolved with longer development of SU-8. The bonding grew from 50 % of the islands bonded to 99.2 % of the islands bonded.

Then, the operating of the chip resulted in leakage due to high pressure. Without epoxy gluing the NISA chip suffered from leakage even at low rates of 1:1 0.01 ml/min. After gluing the tubings at needles and inlets, flow rates up to 0.01 ml/min and 0.4 ml/min (ratio 1:40 and 100 µl/min between islands) were possible to achieve without leakage. In theory, only 10 µm particles should be

found in the product solution. Waste solution is expected to have lower concentration of particles and only 8 µm sized particles in theory. The particles were not seen in outlet samples. Thus, the results from quantitative measurements for particles are not shown. This was because particles did attach to islands as seen in Figure 35. Both microparticles and debris was seen to attach directionally along the flow to PDMS pillars. The surface properties of PDMS are attractive toward negatively charged PS microparticles.

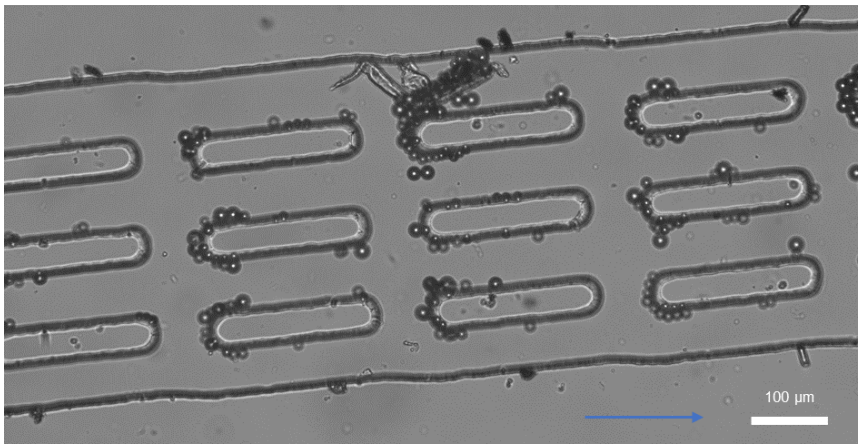

Figure 35 Microparticles attached on NISA islands in 5x brightfield optical microscopic image. Solution consists both 8 and 10 µm particles.

Surfactants, SDS (1 wt-%) and Triton-X (1 wt-%), were investigated to prevent particle attachment. After surfactant experiments, the channels were inspected for particle attaching and this was not seen. However, the low volume fraction of outlet solutions made our developed optical microscopic counting regime inadeaquate for the NISA chip separation characterization. Additionally, SDS solutions led to grainy images in dark field mode and in more false signals in counting macro than detected particles. Triton-X was more effective in imaging. Using SDS gave an opportunity to visualize the flow and gradient throughout the chip and we saw clearly with SDS that the buffer solutions started to back flow towards feed syringe. The buffer solution flow rate causes high enough pressure to achieve this. Thus, lowering pressure at the outlets can be a solution for future optimizations. In these preliminary experiments, there were challenges with flow rate and pressure optimization and low volume fraction of outlet samples. Thus, NISA chip was discarded for being too demanding to optimize within the timeframe and the range of this thesis.

5.2 Concentrator chip

We replicated the Concentrator design from the Martel et al. (40). The chip was fabricated and bonded effectively in spite of the small features. However, SU-8 had some cracking on the pattern surface after development as seen in Figure 36 (a and b). Nevertheless, the pattern transfer resulted in clean channels in Figure 36 (c and d). During preliminary experiments with DIW and particles, the concentration was evident even without quantitative analysis.

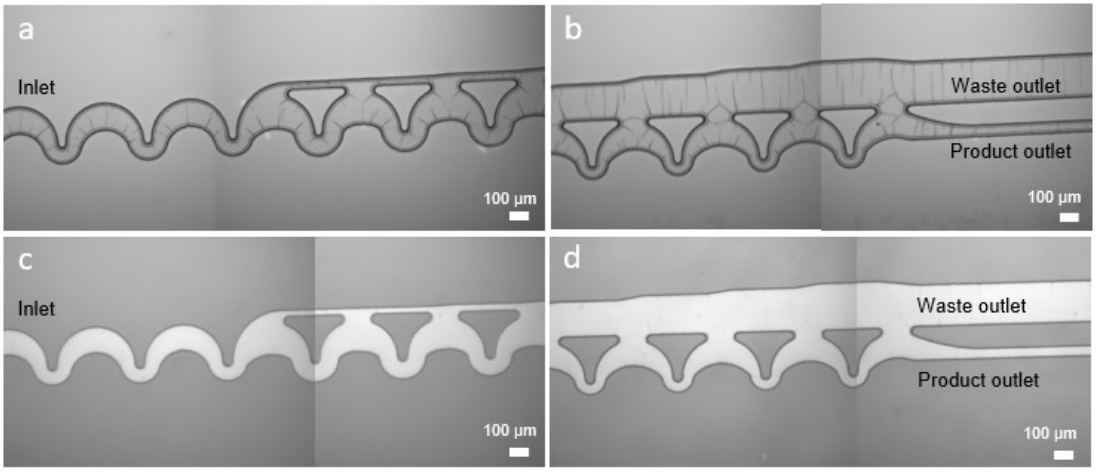

Figure 36 Concentrator chip master and bonded device imaged with 5x brightfield. In concentrator chip, the focusing and siphoning channel gradual changes can be seen from the master (a and b) and the bonded device (c and d). The siphoning channel increases and focusing channel decreases towards the outlets.

According to equation 11, the ratio between particle diameter and channel hydraulic radius characterizes effective inertial focusing, when it is over 0.07 (36), which is achieved effectively in concentrator ship. We estimated that for concentrator chip the ratio for 8 µm particles is 0.24, for 10 µm particles 0.16 and for 15 µm particles 0.13.

During the videoing 0.5 ml/min flow, the particle focusing was visible both using 10^5 and 10^6 particles per ml 10 µm solutions. However, with higher concentration the focusing is apparent and seen in Figure 37. The particles are focused in lower focusing channel while the upper siphoning channel has lower number of particles. There is some particle attachment to channel walls and using the 10^6 particles per ml solution resulted finally in complete clogging of

the channel due to particle attachment. Additionally, we saw in the traces in the channel walls were the focusing line flows during experiments. We speculate that there may be some interaction of particles with the wall during flow, which may be due to high shear rate or deviation from focusing.

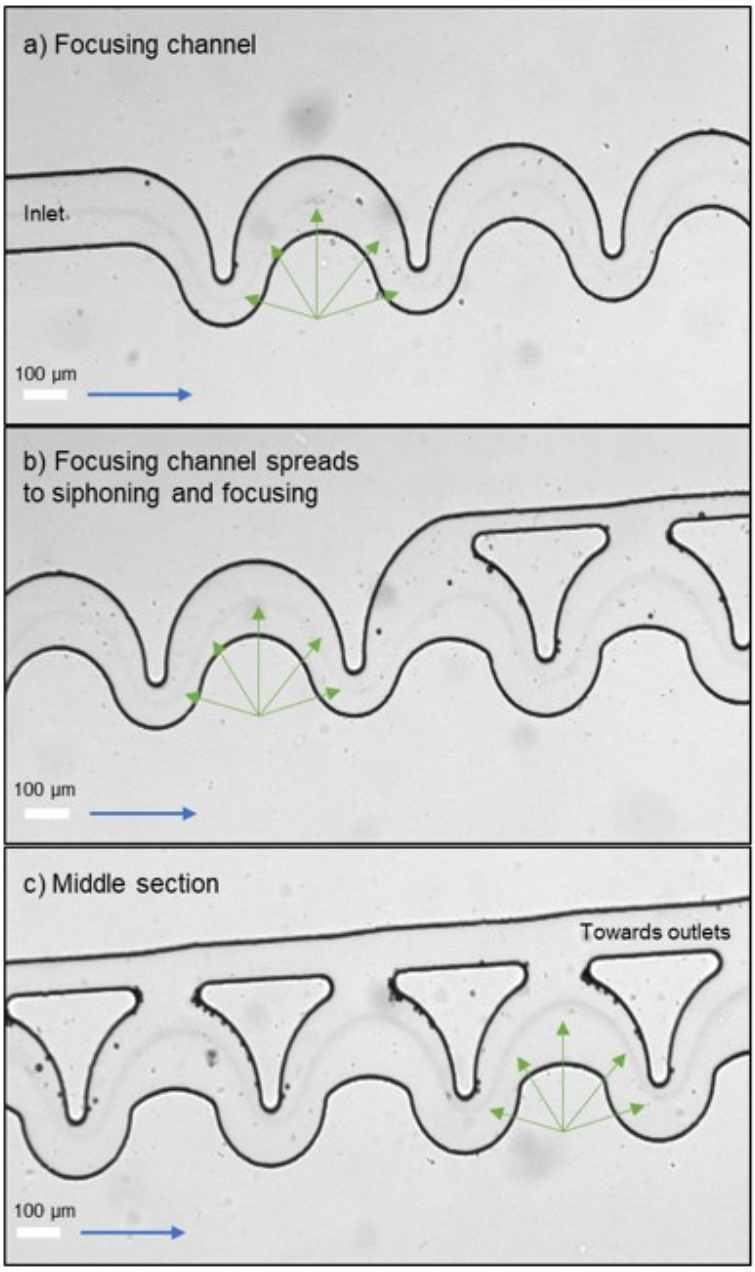

Figure 37 Inertial focusing seen in Concentrator chip with 0.5 ml/min flow rate. Video captures of 10 µm 10^6 particles per ml solution. Blue arrow shows the flow direction and green arrows show the focusing streamline. Focusing starts in the inlet channel (a), continues to separation of siphoning and focusing channels (b). The focusing streamline becomes thicker and darker towards the outlets (c). Siphoning channel remains clear of particles, but islands start to attach particles at the side opposing the flow.

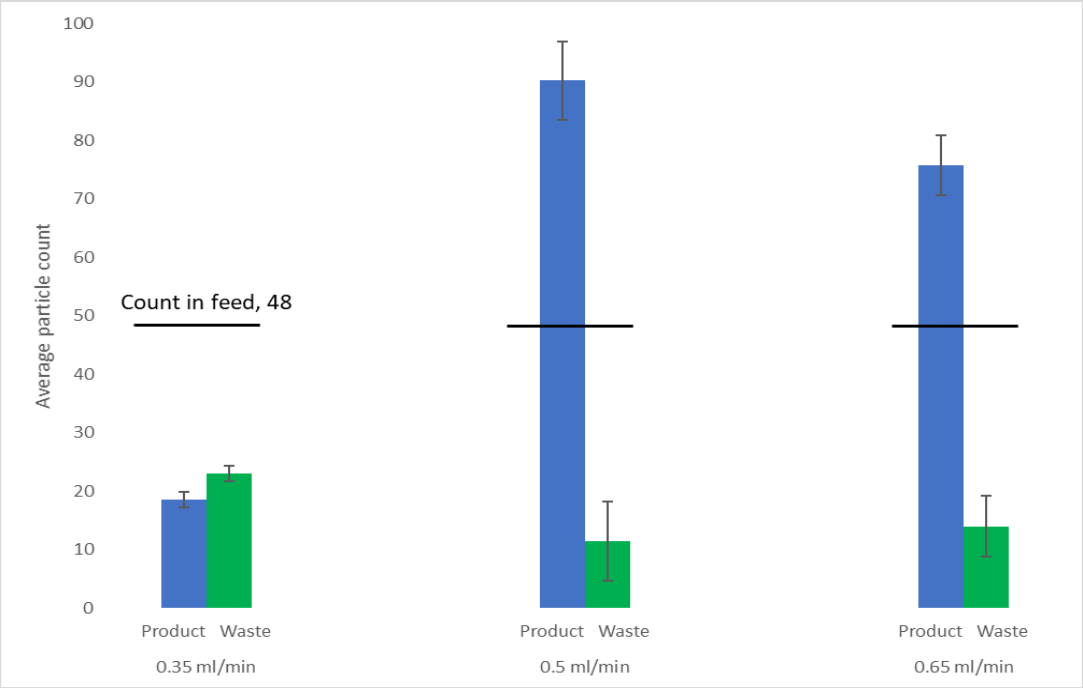

Figure 38 Concentration can be seen both with 0.5 and 0.65 ml/min. Concentrator chip particle counts using solution 10 µm 10^5 particles per ml.

Figure 38 shows the average particle counts of Concentrator chip experiments. Our developed nine image counting method can not determine the concentrations, but we can estimate with particle counts and the volumes of outlet samples (5 ml product, 25 ml waste). Using 0.5 ml/min we were able to gain roughly estimated a 11.3-fold concentration or 7.8 times particles in product than in waste. However, there is a carry-over to waste probably because particles that attach to islands change the focusing geometry and the fluctuation of the flow due to pumps change trajectories. Martel et al. (40) suggested that the optimal flow rate is 0.5 ml/min and our result is in agreement with this. Martel et al. (40) consider that the concentrator has optimal flow range between 0.4 and 0.6 ml/min. In our experiment, 0.35 ml/min resulted in lower overall count of particles and lower yield (Figure 38). According to Martel et al. (40), if the flow rate is lower than 0.4 ml/min, the inertial focusing is not fully developed. This also can explain why the yield is low in 0.35 ml/min, but sedimentation can explain better why the overall count is low as well. Our result of using 0.65 ml/min flow rate resulted in fairly good concentration (Figure 38), but lower than with optimal flow rate. According to Martel et al. (40) larger than 0.6 ml/min causes larger pressure throughout the device and PDMS expands.

Expansion was visually during the experiments and it causes the focusing deviate from the optimal.

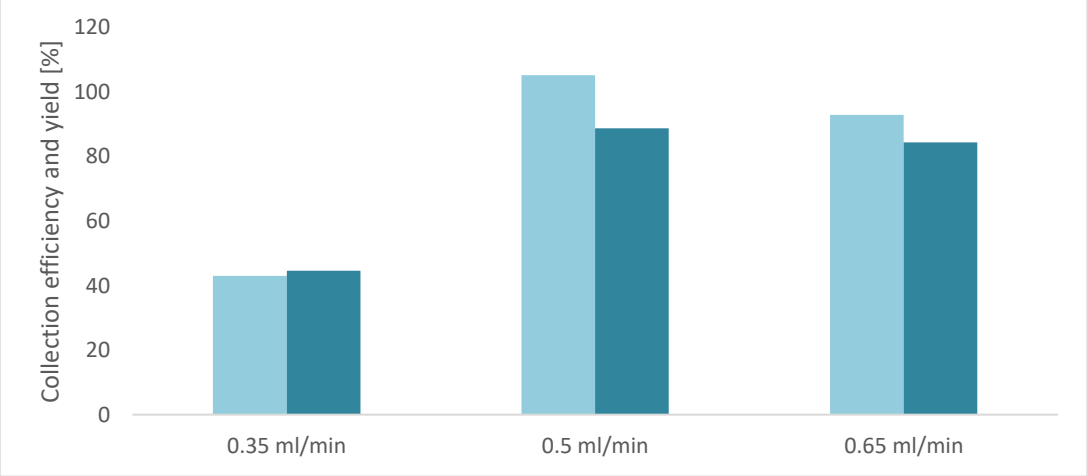

Figure 39 Collection efficiency and yield are better with the baseline flow rate in Concentrator chip. The smallest flow rate gave inefficient collection efficiency and yield, whereas the largest flow rate gave only slightly smaller results than the baseline flow rate.

Concentrator efficiency was calculated using equation 18 (Figure 39). For a concentrator the collection efficiency shows preliminary how the solutions are concentrated in the device. There was volume reduction from 30 ml to 5 ml on average, which is in agreement with the results of Martel et al. (40). The baseline flow rate resulted in 88.7 % yield, while Martel et al. had yield over 95.0 % with 0.4 to 0.6 ml/min range. The differences may be due that our device is not an exact copy of theirs and the sedimentation problems.

We evaluated the device with preliminary set of cell samples of 10^3 to 10^5 in PBS and cell medium. The normalized cell counts in outlet and feed samples are seen in Figure 40 and Figure 41. We gained better concentration results using PBS solutions. It may be the solution property or the low volume fraction in PBS 10^3 cells per ml than 10^5 cells per ml in EMEM. Both preliminary cell solutions gave excellent concentration result using 0.35 ml/min flow rate. This is different from the article results. Martel et al. (40) show that their device of 10x and 50x concentrator works well with 0.5 ml/min up to 10^6 cells per ml white blood cell solutions. The differences may be in deviation due to low number of experiments, inefficient mixing of solutions or inadequate optical

imaging regime. Addition to, we speculate that the shift toward lower optimal flow rate could be due to differences of both the cells and the solute. The deformability of cells changes the focusing positions (2) (20). Additionally, the viscosity of PBS and medium are different from pure DIW, which may lead to lower optimal flow rate. During the experiment we saw that the 0.65 ml/min inlet started to leak due to higher stress from solutions and debris from the medium. Nonetheless, the results are indicative.

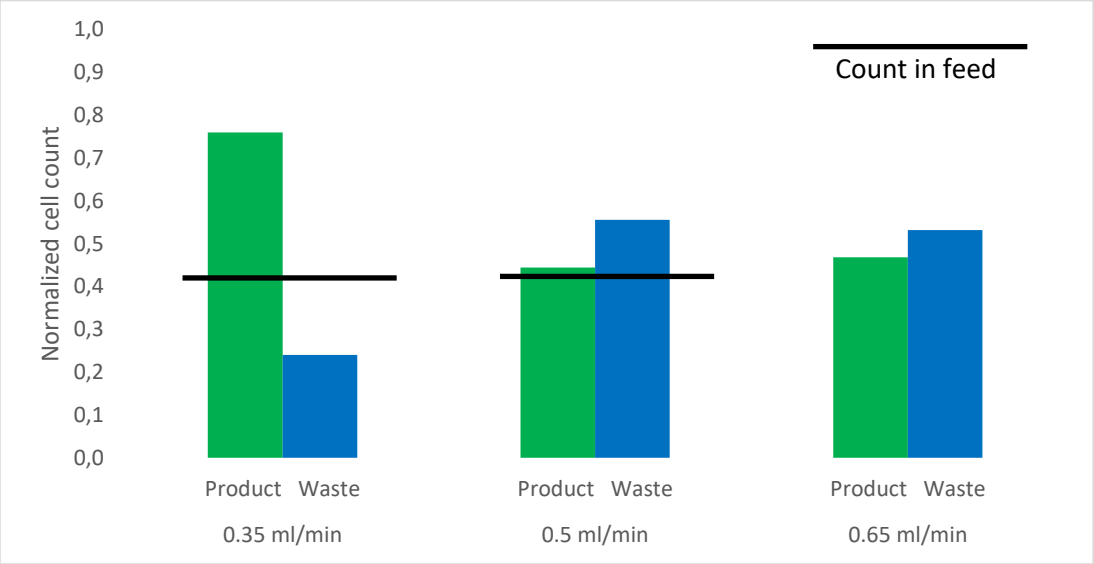

Figure 40 Concentrator chip preliminary cell results with 10^5 cells per ml in medium. The smallest flow rate gave the best concentration results with. Average cell count in feed was different with different experiment days. Averages of nine images.

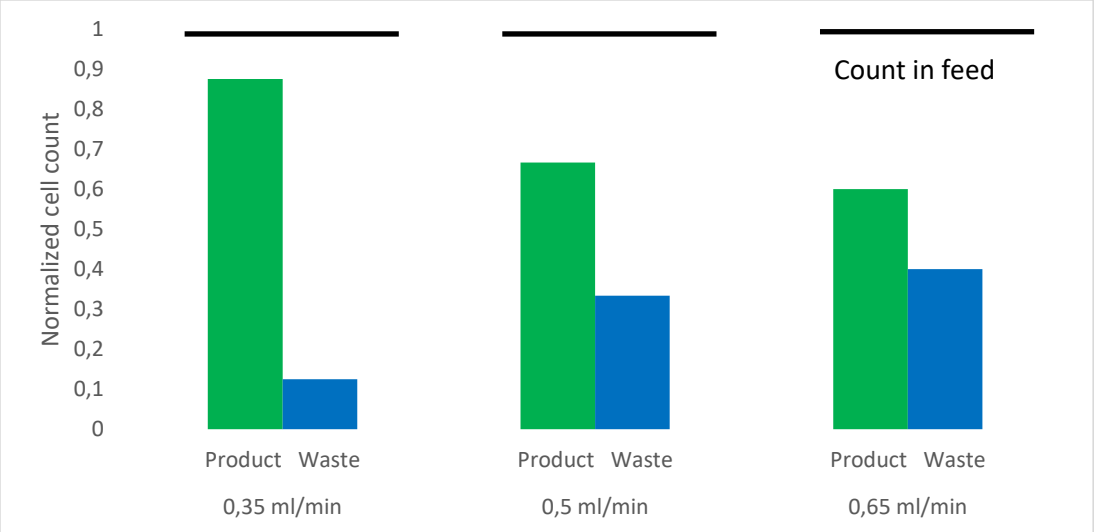

Figure 41 Concentrator chip preliminary cell results with 10^3 cells per ml in PBS. The smallest flow rate gave excellent concentration result, but there is concentration as well with larger flow rates. Averages of nine images.

5.3 Labyrinth chip

Labyrinth chip design was copied successfully from Lin et al. (33) (38). The fabrication of the device was straightforward. The SU-8 pattern with some cracking are seen in Figure 42 (a and b), and bonded channels are clean in Figure 42 (c and d). During device assembly, the outlet between Outer and Middle outlets was left unopened due to space requirements of the tubings.

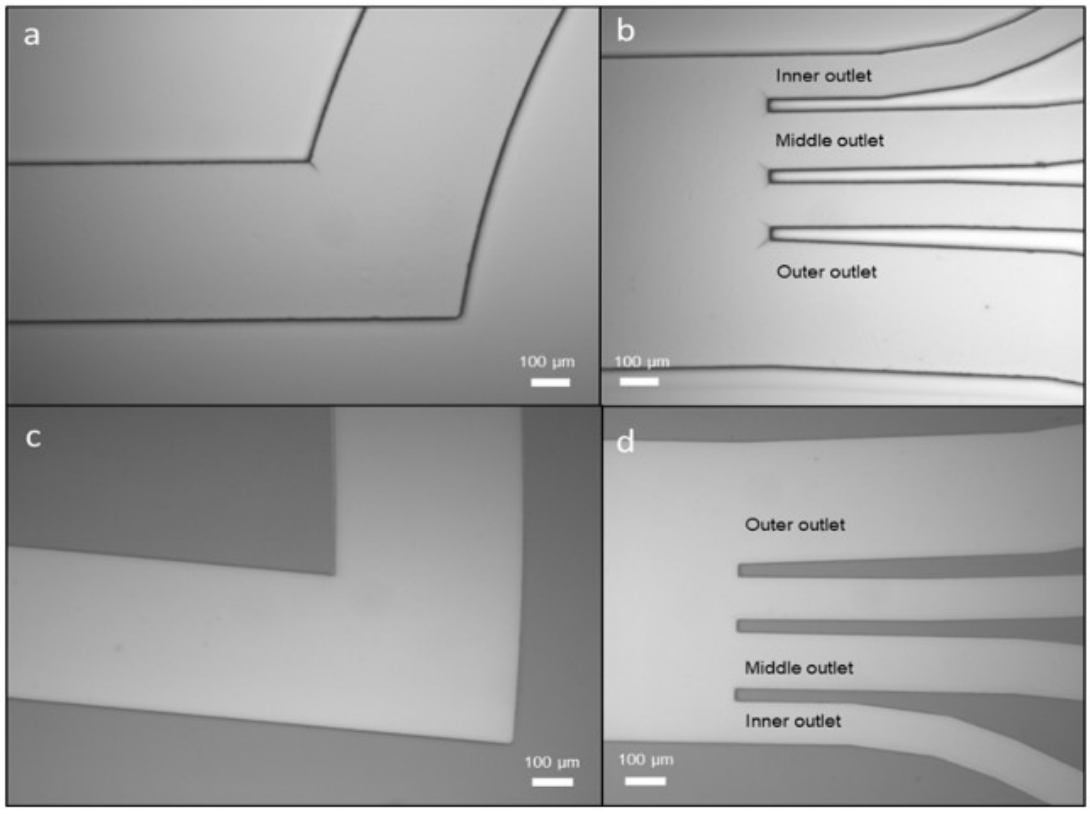

Figure 42 Labyrinth chip imaged with brightfield 5x. Master (a and b) and bonded PDMS on glass device (c and d). Images a and c show an example of a corner and images b and d show the outlets. Master has little cracking on the surface and the bonded chips are clean and effectively bonded.

During preliminary experiments with DIW and particles the chip was operable only up to 2.0 ml/min, then the inlet and tubings started to leak. To achieve the designed operating flow rates epoxy gluing was required.

We estimated the ratio between particle and channel hydraulic radius by equation 11. The ratio for 8 µm is 0.05, for 10 µm 0.06 and for 15 µm 0.09. By this estimation, only larger than 10 µm particles should focus in Labyrinth chip and the results of Lin et al. (33), (38) indicates that focusing occurs with CTCs

sized larger than 13 µm. This also means that smaller than ratio of 0.07 would have carry-over. However, the equation 11 may not be applicable in Labyrinth chip due to the corner induced mixing.

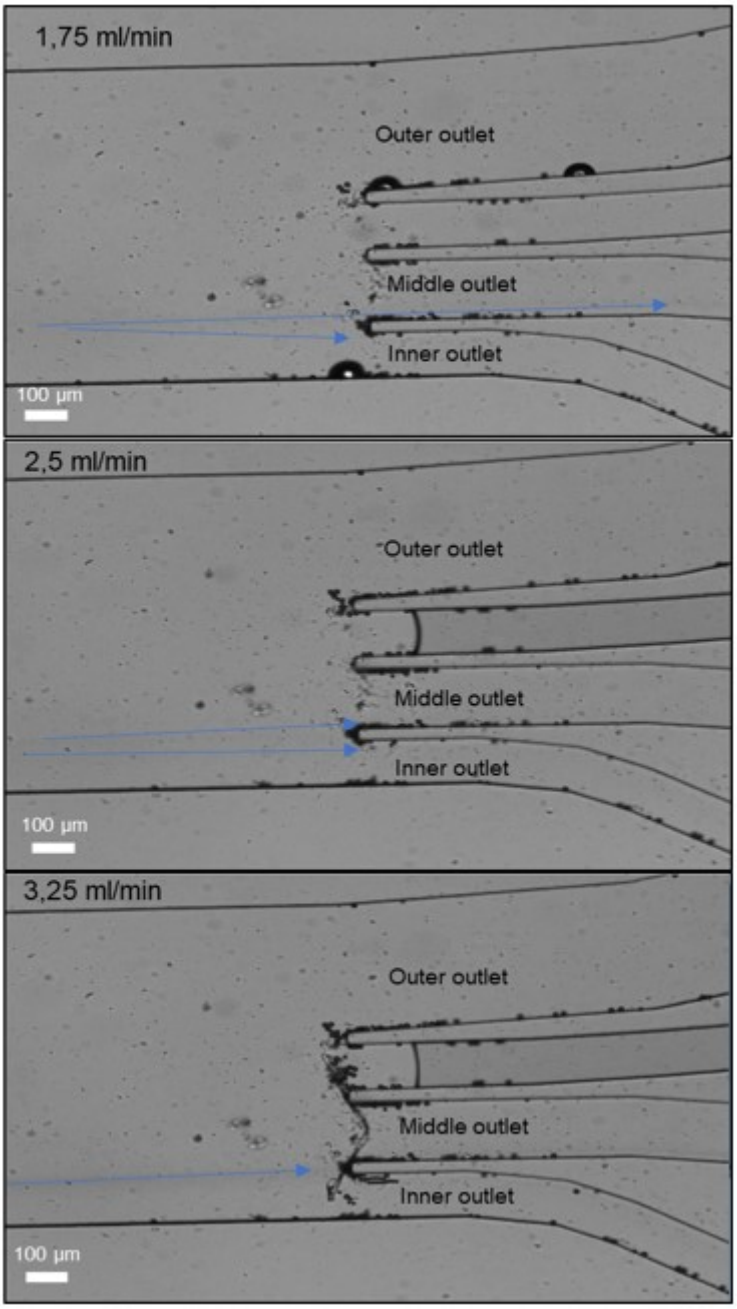

Figure 43 Video captures of Labyrinth chip in 5x brightfield. The inertial streams of particles are seen in videos with blue arrows guiding the eye to show where the particles are flowing. The video shows that there is focusing, but the stream trajectories are straight toward the wall between Inner and Middle outlets. Separation can not be seen in videos. Feed solution 10 µm and 15 µm particles 1:1 10^5 particles per ml.

During video experiments we saw how the particles behaved with different flow rates as seen in Figure 43. In the captures of video, the focusing streams can be detected. Approaching the outlets, the lines become sharper and they approach the Inner outlet. The hydraulic resistance of an unopened outlet may change the focusing and separation radically. Additionally, it was seen that the streams were focused directly to wall between Middle and Inner outlets, which could be prevented with sharper wall design. The focusing of the particles can be seen as well in the Figure 44 with flow rates of 2.5 ml/min and 3.25 ml/min.

Our nine image counting method showed only slight separation of sizes between Inner and Middle outlets (Figure 44). The baseline flow rate to separate the particles has some correlation to the article results. The 15 µm particles have higher count in Middle outlet and 10 µm particles have higher count in Inner outlet. Lin et al. (33), (38) showed that the WBCs (smaller particles) flow to Inner outlet and CTCs (larger particles) to Middle outlet. The difference might be due to unopened outlet, differences between cells and particles, or the cutoff between 10 µm and 15 µm particles versus WBCs (8 to 11 µm) and CTCs (13 to 25 µm) sizes reported by Lin (33).

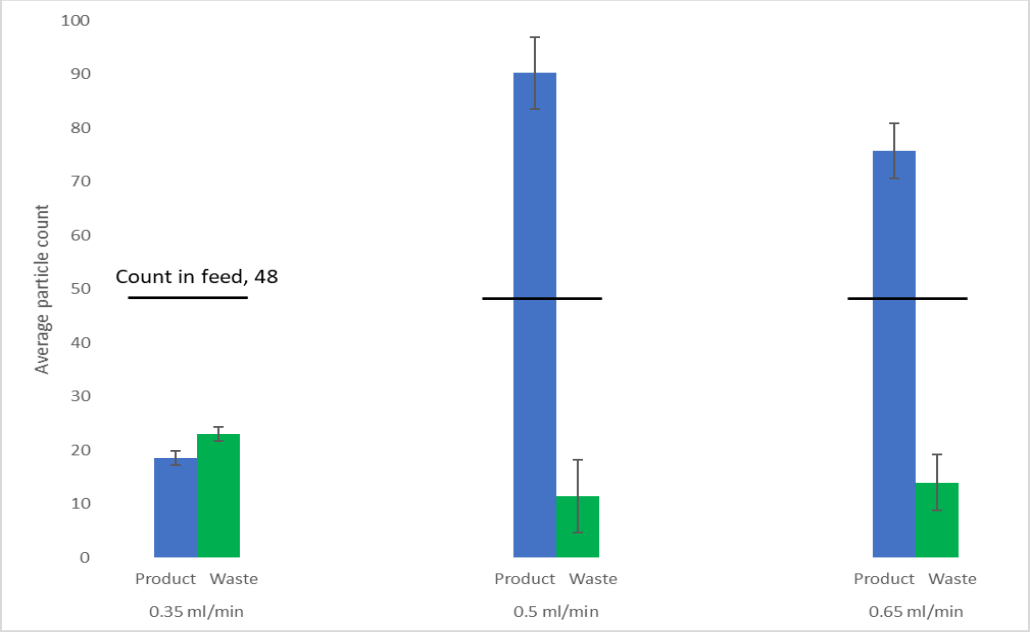

Figure 44 Average particle counts in Labyrinth chip. Both focusing and slight separation can be seen with 2.5 ml/min and 3.25 ml/min. Count in feed is the average number of one size in feed solution. Feed solution 1:1 10 µm and 15 µm 10^5 particles per ml.

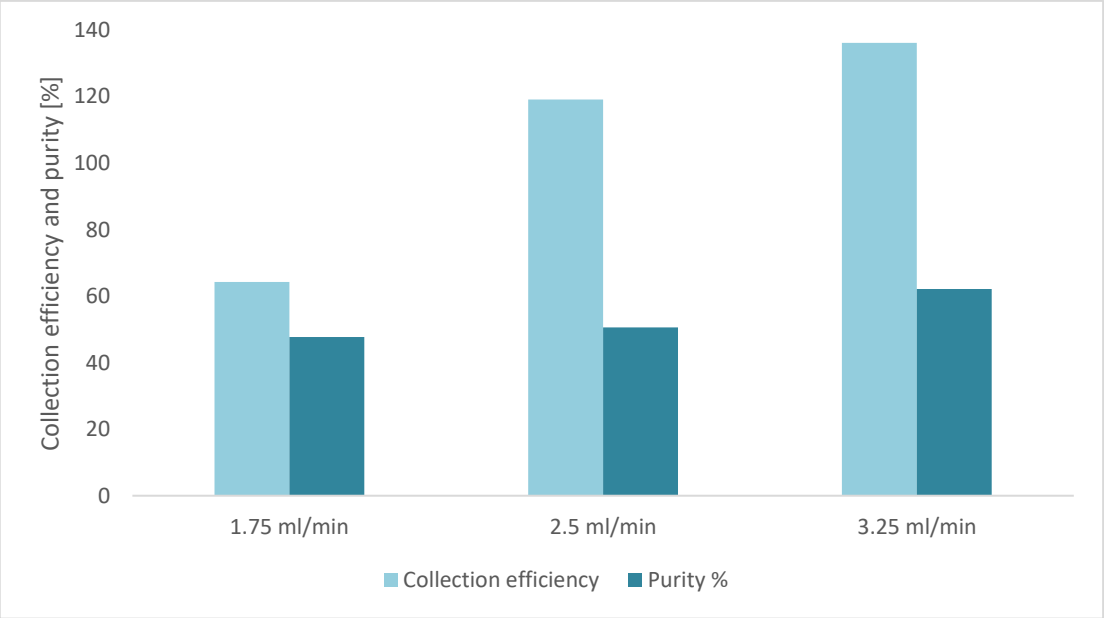

Figure 45 Flow rate increase improves the collection efficiency while purity is rather independent of flow rate in Labyrinth chip.

In Figure 45, can be seen, that the flow rate influences the collection efficiency of 15 µm particles. Labyrinth chip had neither the problem of particle adhesion due to moderately large flow rates and large geometry, cross-section of 100 µm x 500 µm. The deviation may be due to low concentrations of both feed and outlet samples. It may be that our developed nine image counting method is more reliable using higher concentrations. Sedimentation may also influence, because the efficiency is clearly flow rate dependent.

Preliminary cell experiments with medium and PBS are shown in Figure 46 and Figure 47. PBS experiments have some correlation to microparticle results at 1.75 and 2.5 ml/min. However, with the cell medium, the cells preferred the middle outlet in 1.75 and 2.5 ml/min. On the other hand, this result is in better agreement with the Lin et al. (33), (38) results due to by size the trophoblasts are expected to flow to Middle outlet. With 3.25 ml/min for both EMEM and PBS the cells were focused toward Outer outlet even though this was not seen in particle experiments. This may be the properties of the solution or cell deformability. However, we speculate that there is less influence on the results due to cell and solution visco-dynamical properties due to large cross-section and long channel of the device.

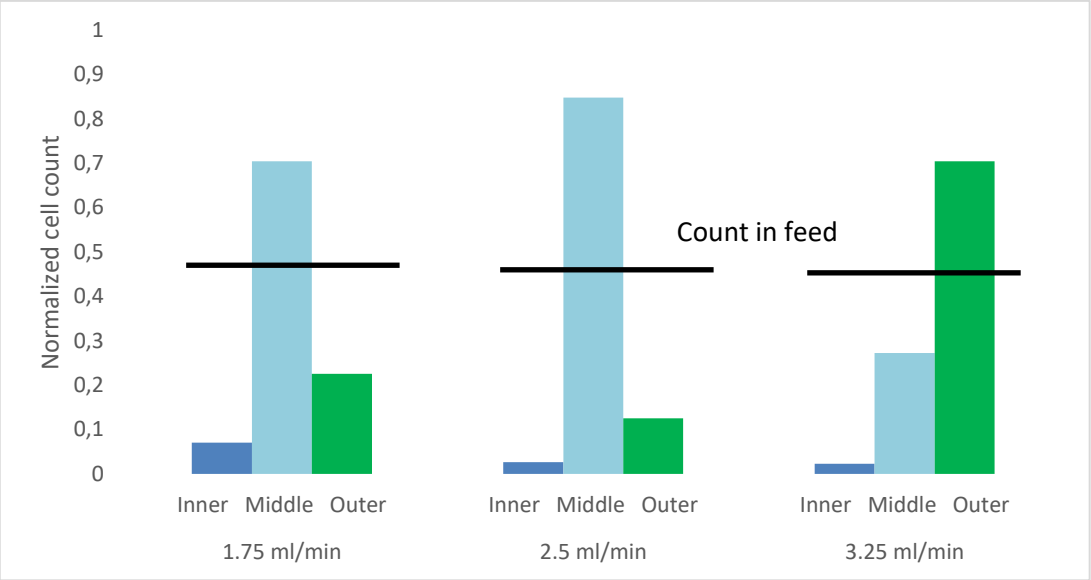

Figure 46 Preliminary cell experiments with cell medium 10^5 cell per ml in Labyrinth chip. Inertial focusing is seen in low and baseline flow rates toward Middle outlet. Trophoblast by size should be going the Middle outlet. With higher flow rate the particles are focused toward Outer outlet. Averages of nine images counts.

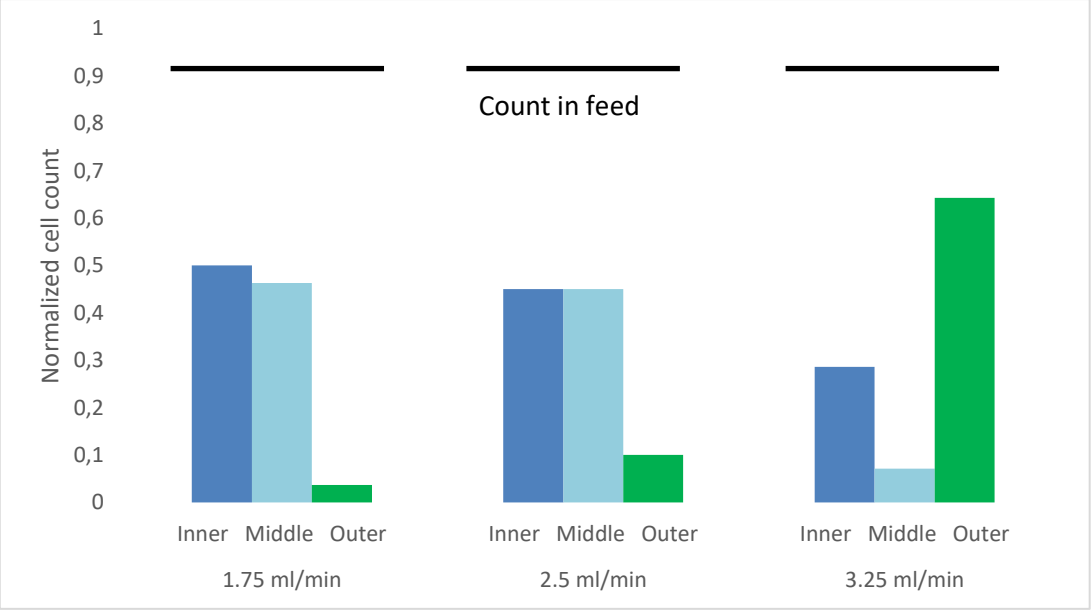

Figure 47 Preliminary cell experiments with PBS $5*10^4$ cells per ml in Labyrinth chip. Inertial focusing is seen in low and baseline flow rates, but toward both Inner and Middle outlets equally. This is in agreement with particle experiments. With larger flow rate the focusing is toward Outer outlet. Averages of nine images counts.

5.4 Spiral chip

Spiral chip was replicated from Shen et al. (31) design. Fabrication of spiral was straightforward. Although some outlet features required further development due to sharp tips of the outlets in the master, seen as darker areas in Figure 48b. Ridges were efficiently transferred and bonded (Figure 48 a and c). Due to space restrictions in outlet designs, we were able to open only three of the seven outlets, named Inner, Middle and Outer.

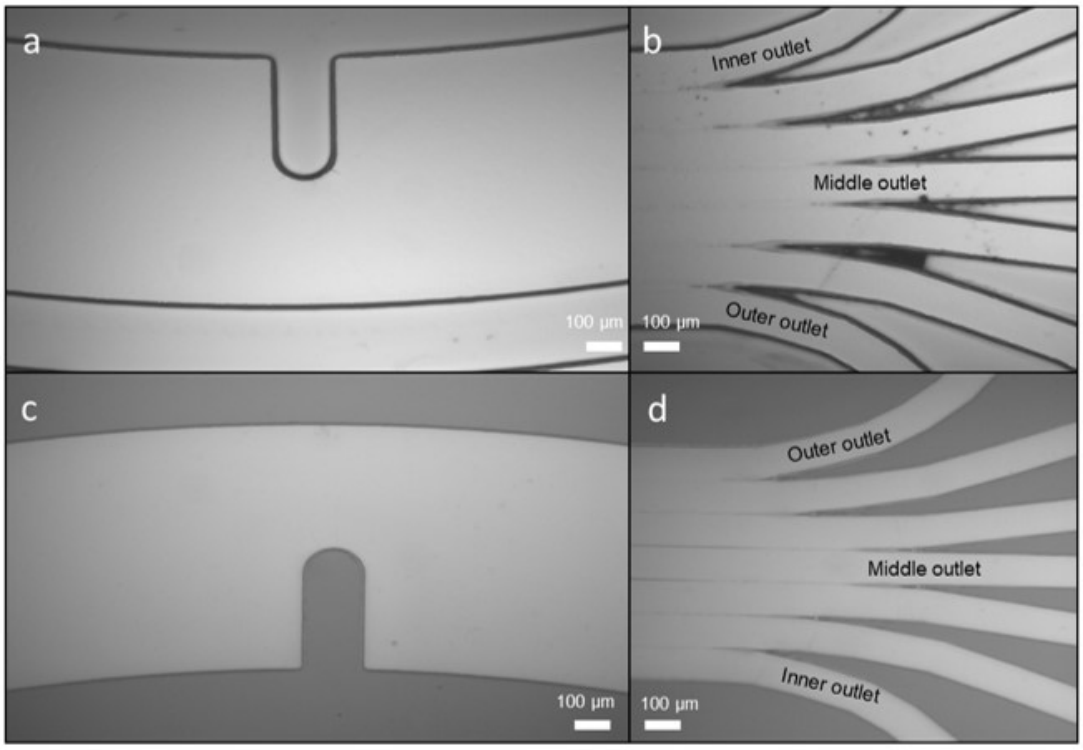

Figure 48 Spiral chip SU-8 master (a and b) and bonded PDMS on glass - device (c and d) imaged with 5x brightfield. Images a and c show one of the ridges and images b and d show the outlets. Only opened outlets are named.

During preliminary flow experiments, there was no leakage. However, the unopened outlets seemed to cause clogging and the device required rinsing after usage to both directions (inlet toward outlet and vice versa). The spiral channel is in the range of ratio of particle versus channel hydraulic radius = 0.07 (equation 11). We estimated that the 15 µm exceeds this (0.08), while 10 µm and 8 µm do not (0.05 and 0.04). The focusing does occur for all sizes (31) propably due to Dean vortices and additional vortice enhancing by the ridges.

We investigated the device with solution of 1:1 10 μm and 15 μm 10^6 particles per ml in DIW. The flow rates were chosen in the region where article of Shen et al (31) promise douple-focusing occuring for both 9.9 μm and 15.3 μm particles. Our estimation for the baseline flow rate was 7 ml/min (Re ~450) and additionally, Shen et al (31) used 6.5 ml/min for a successful experiment with cells.

The video results (Figure 49) are indicating that the device does focus particles to different streams. However, unopened outlets resulted in altered streamlines than in a device with opened outlets (31). The streams tend to be directed toward opened outlets and avoid going toward the unopened outlets. The video captures also indicate as does Shen et al. (31) that the particle streams change positions toward the centre of the channel, when the flow rate increases. The particles as well as cells are supposed to be focused by size so that the smaller particles move toward the centreline of the channel due to stronger influence by the Dean secondary flow. We saw one to several different streams in the videos and speculate that the larger particles are in the streamline closest to the inner outlet.

We determined the average counts of particles using our developed nine image counting method. The results for three different experiments are averaged in Figure 50. There is clear difference in how the particles are separated to Inner and Middle outlet using baseline flow rate of 7 ml/min. In our work the 15 μm particles have a higher count in the Middle outlet and 10 μm particles have higher count in the Inner outlet. This however, is not in agreement with the results of Shen et al. (31). We speculate that altered streamlines seen in video captures (Figure 49) and the clogging during experiments due to unopened outlets have influenced the results. Additionally, our developed counting method may influence the results, especially with the smaller volume fraction samples such as 5 ml/min Outer outlet.

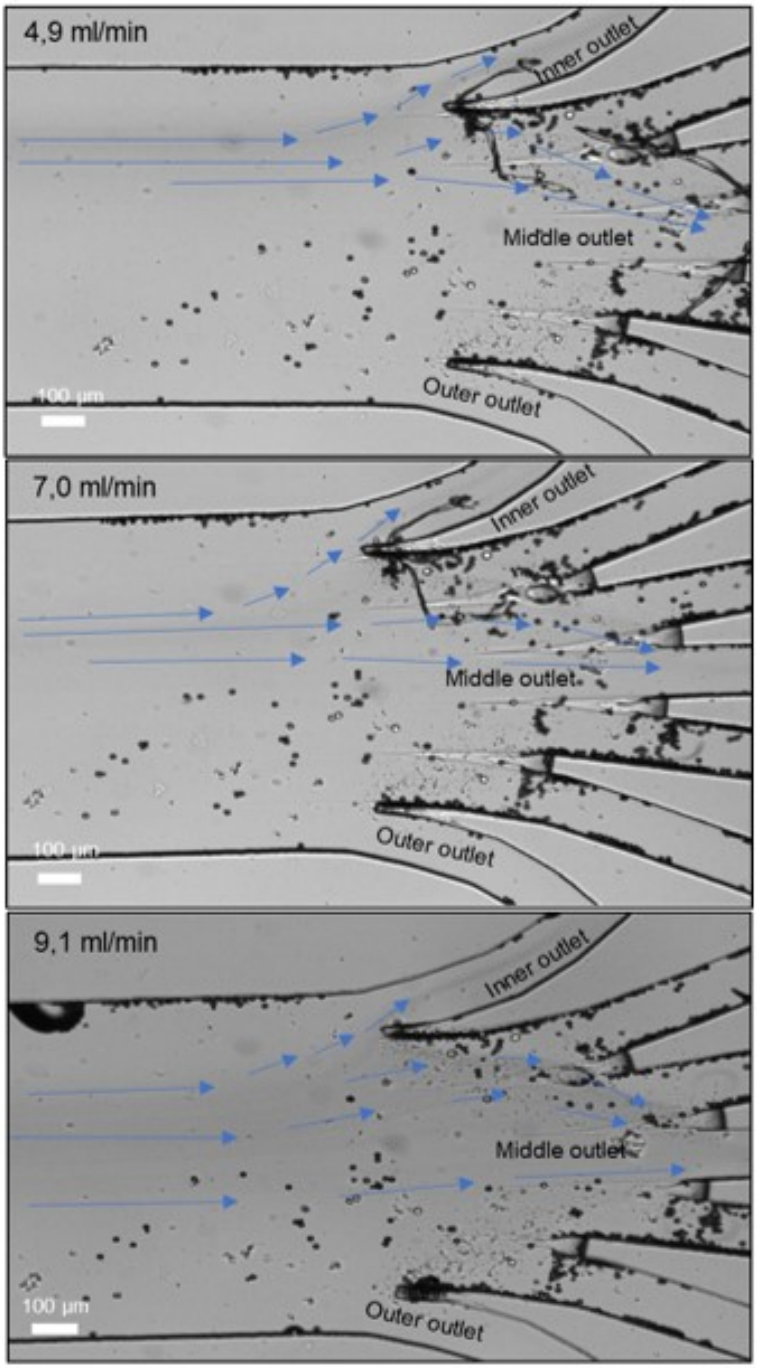

Figure 49 Video captures of Spiral chip PS microparticle experiments 10 µm and 15 µm 1:1 10^6 particles per ml in DIW. At 4.9 ml/min the particles are focused sharply to smaller area and flow toward Inner outlet. At 7.0 ml/min the streamline is wider and shifted toward centreline. They also concentrate toward Middle outlet. At 9.1 ml/min the particles are focused into several streamlines in centreline region and the shift is toward Outer outlet. Inertial streams of particles are visible in bright field 5x. Blue arrows show the direction of streamlines.

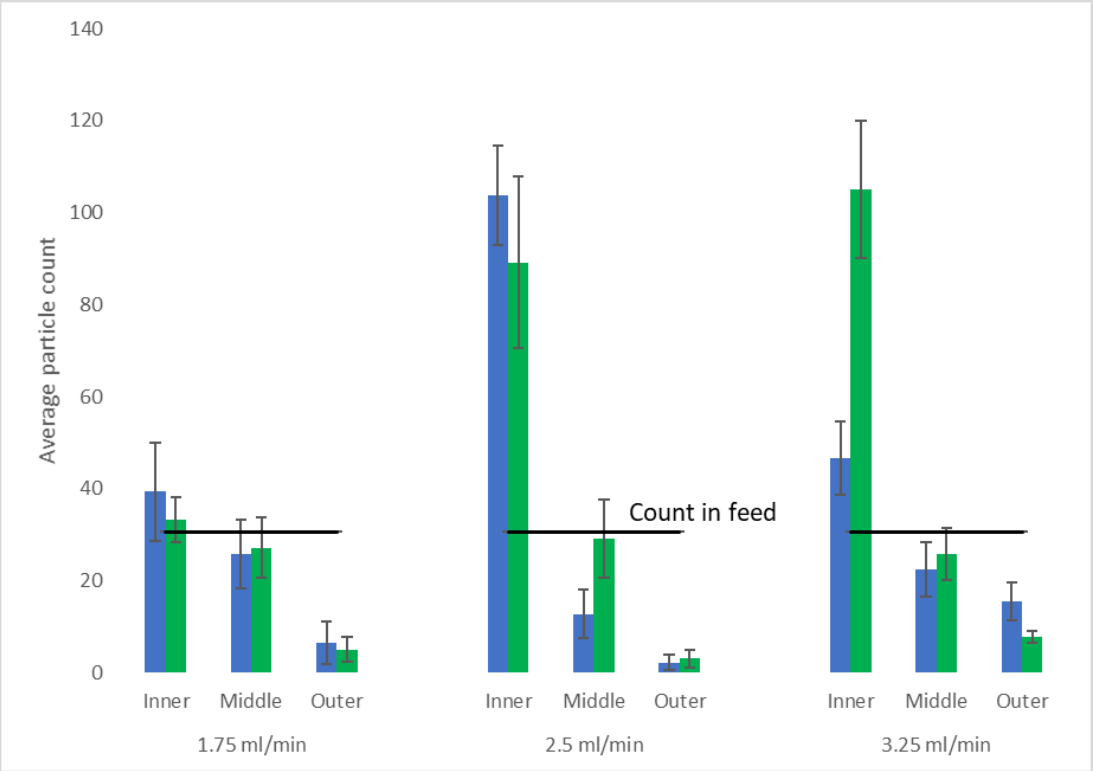

Figure 50 Average microparticle counts from outlet samples in Spiral chip experiments. The shift from Inner outlet toward Outer outlet is seen in increasing the flow rate. The inertial focusing is occurring with each flow rate. Particle separation is clearest with baseline flow rate of 7 ml/min. Feed solution is 10 µm and 15 µm 1:1 10^6 particles per ml. Count in feed is the average number of particles.

We can also see from Figure 50 that the particle focusing shifts from Inner outlet in 4.9 ml/min, to Middle outlet in 7 ml/min toward the Outer outlet in 9.1 ml/min. Shen et al. (31) saw in their work different states for different flow rates. By their work we can speculate that using 4.9 ml/min we achieve State 2, where focusing occurs near the Inner outlet, but no significant separation is occurring. At 7 ml/min we achieve State 4, which is optimal for separating 9.9 µm from 15 µm. At 9.1 ml/min, by Shen et al. (31) work we have achieved State 5, where the particles are in a wide focusing streamline near the centreline of the channel. Our particle measurements show that larger particle have highe count in Middle outlet in 7.0 and 9.1 ml/min and smaller has higher count in Inner outlet with basleine flow rate. These results are inconsistent with article results and are more than likely due to the unopened outlets.

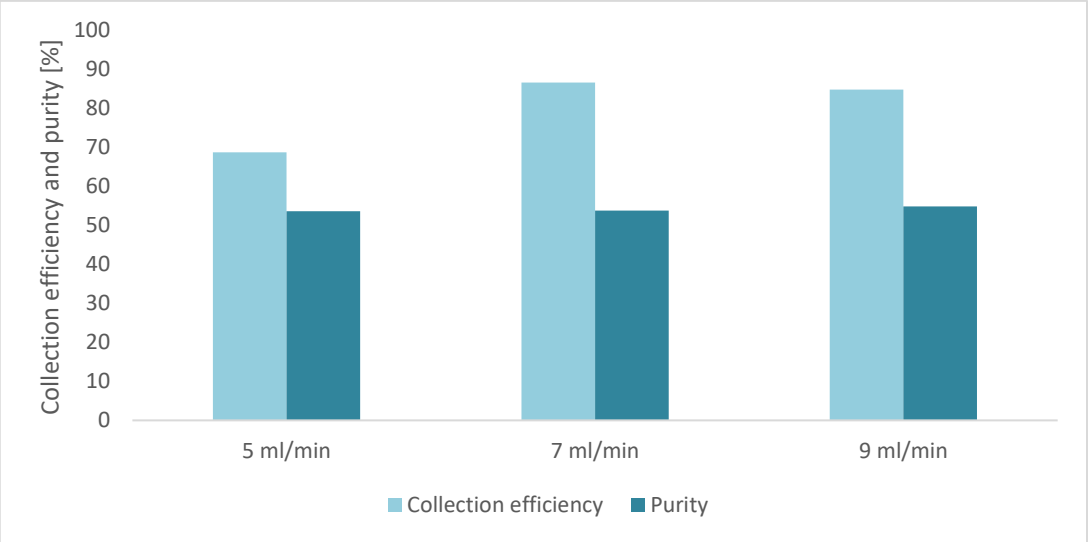

Figure 51 Collection efficiency is not a strong function of flow rate and it is improved with the baseline flow rate. Purity remains constant with each flow rate. Collection efficiency and purity in Spiral chip.

The collection efficiency and purity are shown in Figure 51. Purity remained low for each flow rate, while the collection efficiency was higher for the baseline flow rate.

Preliminary cell experiments are shown in Figure 52 for medium and in Figure 53 for PBS. They seemed to have some correlations between each other even though the different solutions and cell concentrations. There is a trend toward Outer outlet, when flow rate increases. However, the 4.9 ml/min is focusing toward Middle outlet. Trophoblast by size is expected to flow to Inner outlet with both 4.9 ml/min and 7.0 ml/min. According to Shen et al. (31) the larger particles flow to Inner outlet with similar flow rates. The difference may be due to visco-elastic properties of solutions, deformability of cells and slight difference with used flow rates. Clogging is probably not an issue with cell solutions due to small volume fractions. We speculate that sedimentation is not an issue with Spiral chip due to small run times, less than 10 min.

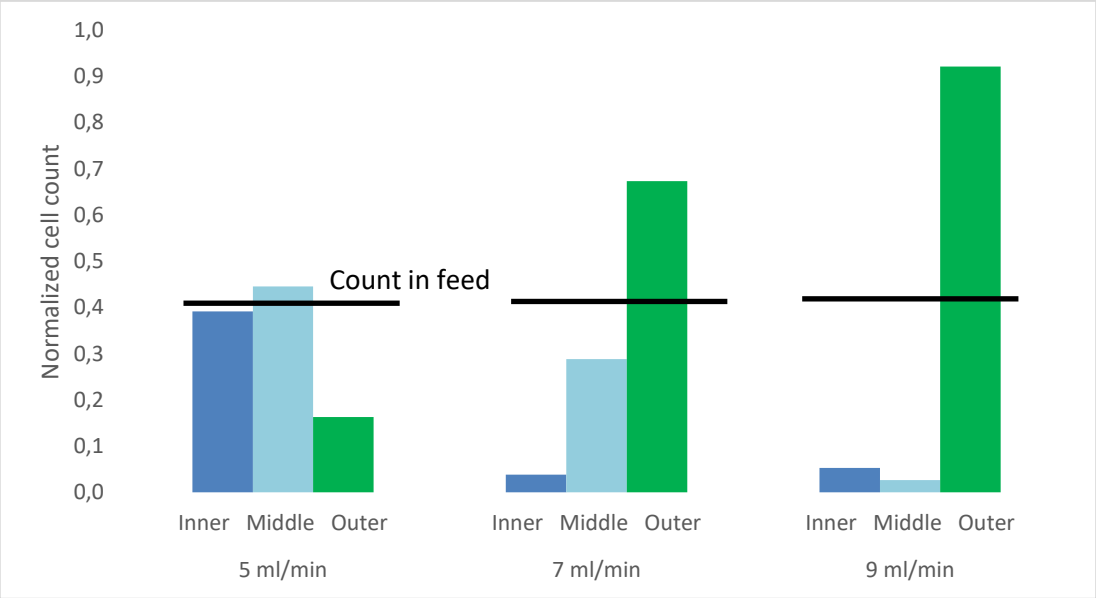

Figure 52 At 4.9 ml/min flow rate the focusing is not evident. The inertial focusing is seen shifting toward Outer outlet in with increasing the flow rate. Spiral chip using Medium 10^5 cells per ml.

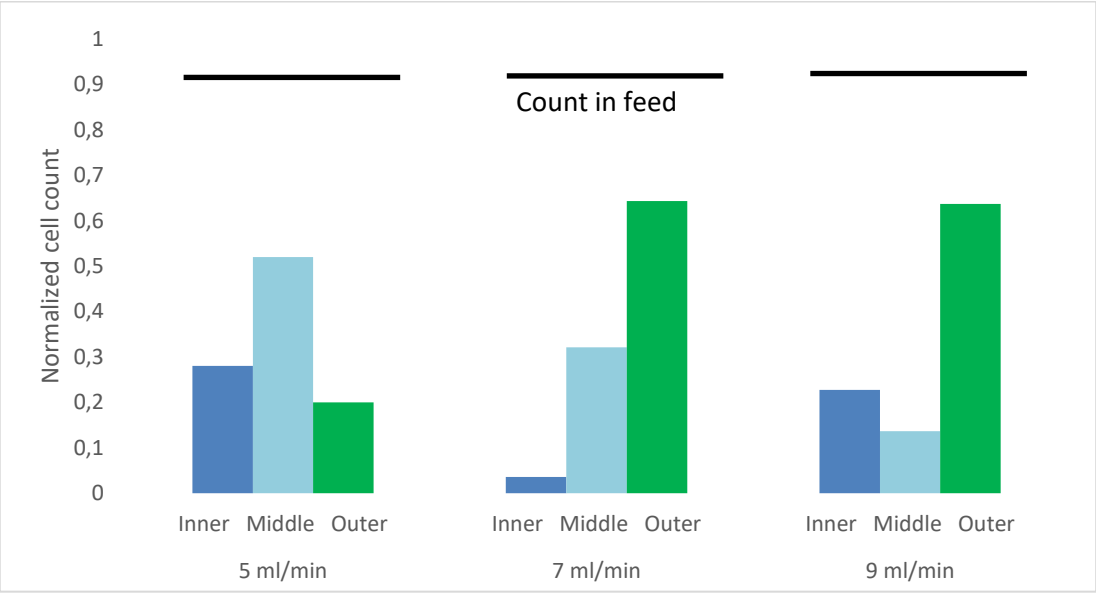

Figure 53 At 4.9 ml/min flow rate the inertial focusing is toward Middle outlet and the shift toward Outer outlet is dependent on increasing the flow rate. Spiral chip using PBS $5*10^4$ cells per ml.

5.5 Optimization issues

During testing several technical issues were resolved. Each device required optimization for own different outlets, solutions and operating. However, there were issues affecting all devices, which are discussed in this chapter.

Particles and cells are in a suspension, but not colloid. This results in several different problems, when investigating with stable flow from a syringe pump, where syringes are in a horizontal holder. Particles in solutions tend to settle down to the other side of the syringe due to gravitation. To address the sedimentation, increasing density of the solvent by dissolving salt was tested. Sedimentation of particles was seen in syringes within 20 min of visual testing with no salt solution of 10 µm ~10^7 particles per ml. The maximum run times for devices with 30 ml sample were for Spiral chip 6 min, for Labyrinth chip 17 min, for the Concentrator for 85 min and for NISA chip 130 min. The influence of sedimentation would explain the lower counts in lower flow rates. Salt solution of 2,5 wt-% salt was tested both visually and thru Spiral chip. Salt slowed down the sedimentation ~10 min, but led to major clogging in Spiral device (Figure 54). Thus, salt was discarded. Sedimentation was prevented during experiments with fast solution preparations. During imaging of the outlet and feed samples the sample vials were mixed vigorously and pipetted using the same method.

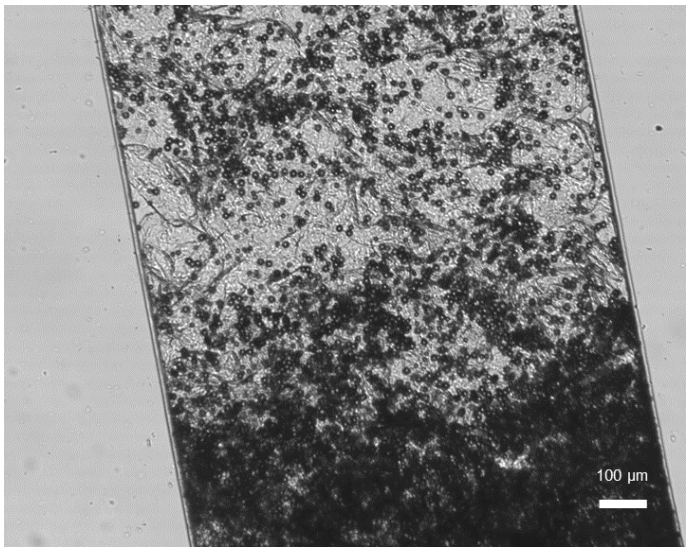

Figure 54 Salt grains are visible in a clogged channel of Spiral chip

5.6 Microparticle separation verification methods

The experiments required a method of counting particles and cells. In this chapter we describe the experiments with Laser Diffraction, Optical microscopy and out developed nine image counting method.

5.6.1 Laser Diffraction

Laser diffraction as a method was proven to be ineffective in determining the concentration and the size distribution of our samples. The method was shown to work for higher concentrations even if the obscuration was lower than 5 %, that was minimum requirement for accuracy. When tested with known concentrations, the method seemed to be working with single particle size. However, with lower concentrations, lower volumes and different sized particles present, the method proved to be inaccurate. In Figure 55, we plotted the results of Malvern 2000 Laser diffraction data of 10 µm and 15 µm particle size distributions. These resulted in wide peaks, whereas two distinct peaks for both sizes would have been preferable. Samples with only one particle size were much more accurate. Laser Diffraction was discarded as a method of particle analysis due to samples having low concentration and volume.

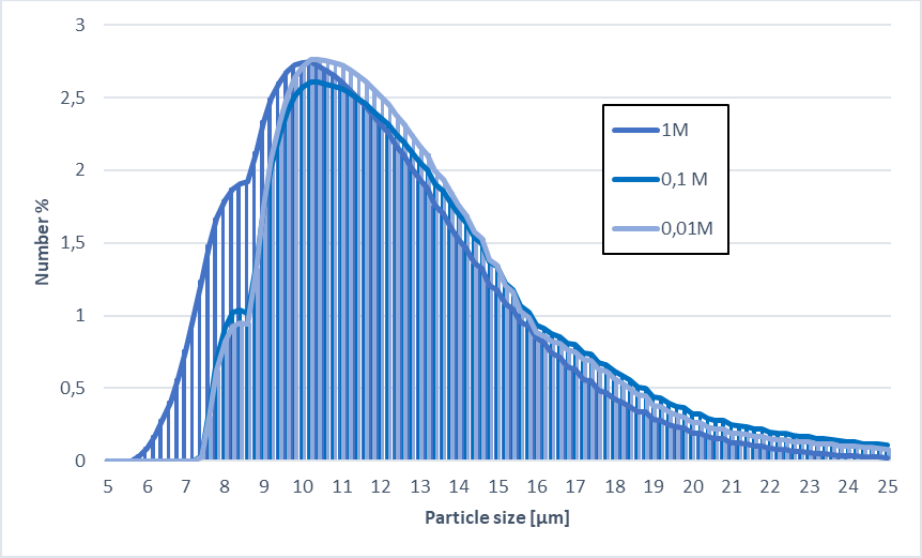

Figure 55 Laser Diffraction method gives size distribution, but not two distinctive peaks for 10 µm and 15 µm sizes. Result of solutions of 1:1 10 µm and 15 µm with three different concentrations.

5.6.2 Developed nine image counting method

Our developed nine image counting method required testing with different optical microscopes, dark vs brightfield modes, droplets and grids. Drying of the samples in air was tested and it led particles to agglomerate, which was inefficient for particle analysis. Then a droplet of 1-6 µl was tested between 2 thin microscope slides. Using this method, the plane of focus in microscope could be kept adequately similar. 3 µl was used for the actual tests because of small amount, but large enough to cover the grid. Concentration of particles was highest in the spot of pipetting, however there were no significant agglomerations present. To obtain statistical accuracy a grid was used to guide imaging. Grid of 1 cm x 1 cm with 3x3 frame was tested with different of paper and transparency. The transparency was proven to show less false signals from the background using ImageJ. Additionally, a glass slide with gold sputtered grid was tested and the gold reflected too much light during imaging and resulted in insufficient particle analysis.

Using dark field instead of bright field highlighted the PS particles, which makes the contrast easier for the software to detect. Our final method consisted dark field mode using a 3 µl droplet between two thin slides on top of a transparency grid 1 cm x 1 cm, 3 x 3 images. All nine grid fields were imaged from the center and analysed with macro developed with ImageJ. Our developed method was effective for higher (10^6 particles per ml) concentrations. However, the results consisted errors and noise.

5.7 Preliminary Cell experiments

Cell tests were run only single time each experiment using different Medium and PBS concentrations from 10^3 to 10^5 cells per ml. There was inconsistency in the preliminary feed count during measurements either due to cell viability or ineffective imaging regime. Feed count in medium reduced by time whereas the PBS feed count grew in time due to measurement errors.

In Figure 56 and Figure 57 are cells used in the preliminary experiments. Approximations of the cell sizes are from 10 µm to 40 µm. Size of the cells seemed to have high distribution and they did agglomerate. This was not quantitatively measured. PBS solutions were easier to work with during testing. It had practically no clogging. Medium solutions instead had big particles of the medium that was not dissolved completely during the mixing of the solutions. This resulted to major clogging especially in Concentrator and Spiral.

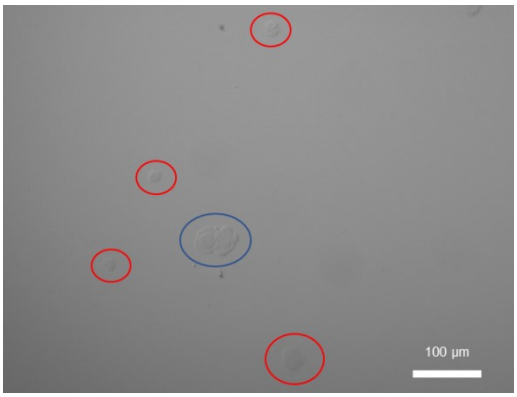

Figure 56 Several JEG-3 cells and a cluster of cells. 10^5 cells per ml in medium, 7 ml/min outer outlet of spiral. Brightfield 10x.

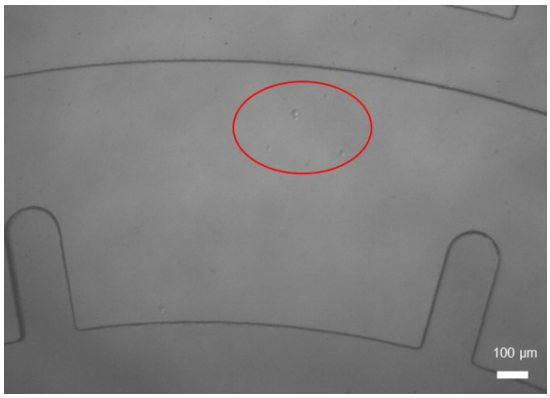

Figure 57 Cells in spiral chip channel after 9 ml/min testing 10^5 cells per ml in medium. 5x brightfield.

In these preliminary experiments, we did not calculate the difference in cell sizes only count of cells. It is an assumption that larger cells, CTCs, WBCs or trophoblasts (>15 µm), would end up in appropriate outlets as seen in literature. Cells were imaged in set of nine images and counts done manually. They were time-consuming to find with the microscope used and testing with the algorithm with same lighting as used in preliminary ImageJ experiments, the algorithm detected multiple false signals or the method would have needed a background correction in the algorithm due to light source giving an uneven contrast to the background.

6 Conclusions and Outlook

Overall experiments showed clear inertial focusing based on observations of particle streams and the significant difference in counts in various outlets. The single line focusing was evident in concentrator chip that additionally showed remarkably effective concentration with 7.8 times particles in product, while reducing the volume five times. The focusing was achieved likewise in Labyrinth and Spiral chips and moreover, the particle results showed some inclination toward separation in Labyrinth chip; 3.5 times more 15 µm particles in Middle outlet than 10 µm particles with 2.5 ml/min. On the other hand, obtaining predictable separation proved to be challenging and the results are indicative. The best result was collected with Concentrator chip; 88.7 % yield, which is slightly less than the 95 % that was reported by Martel et al. (40).

6.1 NISA Chip

We were successful in resolving island bonding and leakage issues in NISA chip. Yet, there was difficulties in optimizing the flow rates and pressure as well as the low volume fraction of outlet samples. For future optimization attempts, we suggest further analysis on devices with sheath-flow. Additionally, surface treatments and surfactants can help to prevent particles and cells from attaching to PDMS. To further analyse and utilize the NISA chip a concentrator attached in series can help to concentrate outlet samples.

6.2 Concentrator chip

The concentrator chip is shown to be effective in both video captures and particle analysis. The device is compact, and parallelization and serialization are both feasible and proven to be working (40) (18) and even commercialized together with NISA chip by Micromedicine (46). Clogging is one of the major drawbacks in the concentrator chip addition to the low volume fraction that it can be operated in. During the designed experiment the baseline flow rate of 0.5 ml/min was collecting efficiently with yield of 88.7 %. Additionally, cell experiments were encouraging; concentration was seen with 0.35 ml/min.

6.3 Labyrinth chip

Inertial focusing was shown to be sharpening toward the outlets of the Labyrinth chip. The mixing effect of corners were not seen during videoing. It was evident that particle trajectories were toward both Middle and Inner outlets, which is in some agreement with the Lin's (33) results and the concept has merits in focusing. We speculated that the deviation was from unopened outlet and particle vs. cell behaviour. We recommend further experiments with a fully opened device using different concentrations of cells, video of fluorescent cells and experimenting on different designs of outlets to achieve optimal separation using cells.

6.4 Spiral chip

The Spiral chip with ridges is extremely high throughput with 7.0 ml/min optimal flow rate operable in low pressure. It was shown that focusing was occurring throughout the device. The clogging we saw was evidently due to unopened outlets and we see great promise in Spiral chip to be optimized for further experiments. We recommend estimations and videoing first the behaviour of fluorescent cells near the outlet to enhance the design of the final outlets. We saw one to several different streams in the videos and speculate that the larger particles are in the streamline closest to the inner outlet. However, the particle analysis did not show any significant separation due to unopened outlets.

6.5 Microfluidic rare cell enrichment

The conventional FACS is still regarded as the powerhouse for enrichment of cells. The shortcomings are a large sample size requirement, low recovery, large footprint of the equipment and high cost. On the other hand, microfluidics offers to overcome these with lower sample sizes, higher recoveries, miniscule device footprint, and smaller manufacturing and operating. Microfluidics provide scaled-down designs suitable for manipulation in size range of cells (1). Many of the research designs require still proof-of-concept experimenting and investing in standardization, manufacturability and repeatable

performance. Major benefits using inertial microfluidics is the high throughput with a possibility to even separate rare cells from native fluids. Additionally, there are advances scale-up innovations of microfluidic chips that can raise the throughput. The significance of our investigated devices is that two of them provide superior throughput of 7 ml/min and 2.5 ml/min, while the other two have been proven to be high-throughput by serialization.

Draw-backs of inertial microfluidics is the breakdown of the separation method and additional clogging using highly concentrated fluids. Moreover, native fluids need to be diluted even though some articles have promised to be able to use undiluted fluid. Zhou et al (14) suggested that with high enough concentration the larger particles focused in a stream would repel smaller particles further away and thus enhancing the separation. Dilution increases the processing time or the purity of fractionated cells (47). Furthermore, we recommend a filtration. There are attempts in literature to try to solve this with hybrid-mechanisms. Both active and passive methods are combined to achieve stable performance, versatility and convenience with stepwise sorting.

Additionally, hybrid microfluidic chip could achieve multiplexed high throughput separation. Optimising a design presented in this work is the first step. Then prototyping different methods for enriching cells from the native fluids, which requires to be operatable in non-newtonian conditions of whole blood and filter out the unwanted parts of blood. Combining passive method with an active one would improve the throughput and offers real-time feedback system to adjust parameters (11). On the other hand, continuous flow-based separation through serialized chip needs to be overcome.

According to the literature review a single microfluidic separation method can not by itself solve the problem of finding a needle in the haystack, but to reduce stepwise the amount of hay. Our results are in line with reducing the amount of abundant cells with reduced loss of rare cells. We recommend finding a stepwise solution for gaining rare cell separation from a native fluid.

References

1. *Microfluidic cell sorting: a review of the advances in the separation of cells from debulking to rare cell isolation.* **Shields IV, C., W., Reyes, C., D., and López, G., P.** 5, s.l. : Royal Society of Chemistry, 2015, Lab on a Chip, Vol. 15, pp. 1230-1249.
2. *Fundamentals and applications of inertial microfluidics: a review.* **Zhang, J., Yan, S., Yuan, D., Alici, G., Nguyen, N-T., Warkiani, M., E., and Li, W.** 1, s.l. : Royal Society of Chemistry, 2016, Lab on a Chip, Vol. 16, pp. 10-34.
3. *Platelet size in man.* **Paulus, J.-M.** 3, s.l. : Am Soc Hematology, 1975, Blood, Vol. 46, pp. 321-336.
4. *BioNumbers—the database of key numbers in molecular and cell biology.* **Milo, R., Jorgensen, P., Moran, U., Weber, G. and Springer, M.** suppl_1, s.l. : Oxford University Press, 2009, Nucleic acids research, Vol. 38, pp. D750-D753.
5. *Biochip for separating fetal cells from maternal circulation.* **Mohamed, H., Turner, J., N., and Caggana, M.** 2, s.l. : Elsevier, 2007, Vol. 1162, pp. 187-192.
6. *Inertial focusing for tumor antigen--dependent and--independent sorting of rare circulating tumor cells.* **Ozkumur, E., Shah, A., M., Ciciliano, J., C., Emmink, B., L., Miyamoto, D., T., Brachtel, E., Yu, M., Chen, P.-i., Morgan, B., and Trautwein, J.** 179, s.l. : American Association for the Advancement of Science, 2013, Science translational medicine, Vol. 5, pp. 179ra47--179ra47.
7. *Measurements of the dielectric properties of peripheral blood mononuclear cells and trophoblast cells using AC electrokinetic techniques.* **Chan, KL., Morgan, H., Morgan, E., Cameron, IT., and Thomas, MR.** 3, s.l. : Elsevier, 2000, Biochimica et Biophysica Acta (BBA)-Molecular Basis of Disease, Vol. 1500, pp. 313-322.
8. *Using fetal cells for prenatal diagnosis: History and recent progress.* **Beaudet, A. L.** 2, s.l. : Wiley Online Library, 2016, Vol. 172, pp. 123-127.
9. *Fetal gender and several cytokines are associated with the number of fetal cells in maternal blood--an observational study.* **Schlütter, J., M., Kirkegaard, I., Petersen, O., B., Larsen, N., Christensen, B., Hougaard, D., M., Kølvraa, S., Uldbjerg, N.** 9, s.l. : Public Library of Science, 2014, Plos one, Vol. 9, p. e106934.
10. *Fetal cells in maternal blood.* **Wachtel, S.S., Shulman, L.P., and Sammons, D.** 2, s.l. : Wiley Online Library, 2001, Clinical genetics, Vol. 59, pp. 74-79.
11. *Hybrid microfluidics combined with active and passive approaches for continuous cell separation.* **Yan, S., Zhang, J., Yuan, D., and Li, W.** 2, s.l. : Wiley Online Library, 2017, Electrophoresis, Vol. 38, pp. 238-249.
12. *Microfluidic technologies in cell isolation and analysis for biomedical applications.* **Wu, J., Chen, Q., and Lin, J.-M.** 3, s.l. : Royal Society of Chemistry, 2017, Analyst, Vol. 142, pp. 421--441.
13. *Isolation of Circulating Fetal Trophoblasts Using Inertial Microfluidics for Noninvasive Prenatal Testing.* **Winter, M., Hardy, T., Rezaei, M., Nguyen, V., Zander-Fox, D., Ebrahimi W., M. and Thierry, B.** s.l. : Wiley Online Library, 2018, Advanced Materials Technologies, p. 1800066.

14. *Sheathless inertial cell focusing and sorting with serial reverse wavy channel structures.* **Zhou, Y., Ma, Z. and Ai, Y.** 1, s.l. : Nature Publishing Group, 2018, Microsystems & Nanoengineering, Vol. 4, p. 5.
15. *Fluorescence activated cell sorting.* **Bonner, W., A., Hulett, H., R., Sweet, R., G., and Herzenberg, L., A.** 3, s.l. : AIP, 1972, Review of Scientific Instruments, Vol. 43, pp. 404-409.
16. **Ratner, B., D., Hoffman, A., S., Schoen, F., J., and Lemons, J., E.,.** *Biomaterials Science - An Introduction to Materials in Medicine (3rd Edition).* 3rd. s.l. : Academic Press, 2013. p. 1573. 9780080877808.
17. *An IB-LBM study of continuous cell sorting in deterministic lateral displacement arrays.* **Wei, Q, Xu, Y.-Q., Tang, X.-Y. and Tian, F.-B.** 6, s.l. : Springer, 2016, Acta Mechanica Sinica, Vol. 32, pp. 1023-1030.
18. *Non-equilibrium Inertial Separation Array for High-throughput, Large-volume Blood Fractionation.* **Mutlu, B., R., Smith, K., C., Edd, J., F., Nadar, P., Dlamini, M., Kapur, R. and Toner, M.** 1, s.l. : Nature Publishing Group, 2017, Scientific Reports, Vol. 7, p. 9915.
19. *Silicon-based microfilters for whole blood cell separation.* **Ji, H. M., Samper, V., Chen, Y., Heng, C. K., Lim, T. M., and Yobas, L.** 2, s.l. : Springer Science, 2008, Biomedical microdevices, Vol. 10, pp. 251-257.
20. *High-throughput rare cell separation from blood samples using steric hindrance and inertial microfluidics.* **Shen, S., Ma, C., Zhao, L., Wang, Y., Wang, J.-C., Xu, J., Li, T., Pang, L., and Wang, J.** 14, s.l. : Royal Society of Chemistry, 2014, Lab on a Chip, Vol. 14, pp. 2525--2538.
21. *Pinched flow fractionation: continuous size separation of particles utilizing a laminar flow profile in a pinched microchannel.* **Yamada, M., Nakashima, M. and Seki, M.** 18, s.l. : ACS Publications, 2004, Analytical chemistry, Vol. 76, pp. 5465-5471.
22. *Continuous flow separation of particles within an asymmetric microfluidic device.* **Zhang, X., Cooper, J., M., Monaghan, P., B., and Haswell, S., J.** 4, s.l. : Royal Society of Chemistry, 2006, Lab on a Chip, Vol. 6, pp. 561-566.
23. *Nanoroughened Surfaces for Efficient Capture of Circulating Tumor Cells without Using Capture Antibodies.* **Chen, W., Weng, S., Zhang, F., Allen, S., Li, X., Bao, L., Lam, R., H., W., Macoska, J., A., Merajner, S., D. and Fu, J.** 1, s.l. : American Chemical Society, 2013, ACS nano, Vol. 7, pp. 566-575.
24. *Inertial microfluidics.* **Di Carlo, D.** 21, s.l. : Royal Society of Chemistry, 2009, Lab on a Chip, Vol. 9, pp. 3038-3046.
25. **Hood, K., T.** *Theory of Particle Focusing in Inertial Microfluidic Devices.* UCLA. Los Angeles : University of California, 2016. Dissertation.
26. *Particle segregation and dynamics in confined flows.* **Di Carlo, D., Edd, J., F., Humphry, K., J., Stone, H., A., and Toner, M.** 9, s.l. : APS, 2009, Physical review letters, Vol. 102, p. 094503.
27. *Inertial microfluidic physics.* **Amini, H., Lee, W., and Di Carlo, D.** 15, s.l. : Royal Society of Chemistry, 2014, Lab on a Chip, Vol. 14, pp. 2739-2761.
28. *High-throughput particle manipulation based on hydrodynamic effects in microchannels.* **Liu, C., and Hu, G.** 3, s.l. : MDPI, 2017, Micromachines, Vol. 8, p. 73.

29. *The inertial lift on a spherical particle in a plane Poiseuille flow at large channel Reynolds number.* **Asmolov, E., S.** s.l. : Cambridge University Press, 1999, Journal of Fluid Mechanics, Vol. 381, pp. 63--87.
30. **Kuntaegowdanahalli, S., S.** *Inertial microfluidics for continuous particle separation in spiral microchannels.* Electrical and Computer Engineering of the College of Engineering, University of Cincinnati . 2009. p. 59, Master's thesis.
31. *Spiral microchannel with ordered micro-obstacles for continuous and highly-efficient particle separation.* **Shen, S., Tian, C., Li, T., Xu, J., Chen, S., W., Tu, Q., Yuan, M., S., Liu, W. and Wang, J.** 21, s.l. : Royal Society of Chemistry, 2017, Lab on a Chip, Vol. 17, pp. 3578--3591.
32. *Ultra-fast, label-free isolation of circulating tumor cells from blood using spiral microfluidics.* **Warkiani, M., E., Khoo, B., L., Wu, L., Tay, A., K., P., Bhagat, A., A., S., Han, J., and Lim, C., T.** 1, s.l. : Nature Publishing Group, 2016, Nature protocols, Vol. 11, p. 134.
33. **Lin, E.** *High-throughput microfluidic Labyrinth for the label-free isolation of circulating tumor cells.* s.l. : AACR, 2018. Dissertation.
34. *Deformability-based cell classification and enrichment using inertial microfluidics.* **Hur, S., C., Henderson-MacLennan, N., K., McCabe, E., R., B., and Di Carlo, D.** 5, s.l. : oyal Society of Chemistry, 2011, Lab on a Chip, Vol. 11, pp. 912-920.
35. *Continuous scalable blood filtration device using inertial microfluidics.* **Mach, A., J., and Di Carlo, D,.** 2, s.l. : Wiley Online Library, 2010, Biotechnology and bioengineering, Vol. 107, pp. 302-311.
36. *Fundamentals of inertial focusing in microchannels.* **Zhou, J. and Papautsky I.** 6, s.l. : Royal Society of Chemistry, 2013, Lab on a Chip, Vol. 13, pp. 1121-1132.
37. *Continuous focusing of microparticles using inertial lift force and vorticity via multi-orifice microfluidic channels.* **Park, J.-S., Song, S.-H., and Jung, H.-I.** 7, s.l. : Royal Society of Chemistry, 2009, Lab on a Chip, Vol. 9, pp. 939-948.
38. *High-throughput microfluidic Labyrinth for the label-free isolation of circulating tumor cells.* **Lin, E., Rivera-Báez, L., Fouladdel, S., Yoon, H. J., Guthrie, S., Wieger, J., Deol, Y., Keller, E., Sahai, V., Simeone, D. M., Burness, M. L., Azizi, E., Wicha, M. S. and Nagrath, S.** 3, s.l. : Elsevier , 2017, Cell systems, Vol. 5, pp. 295-304.
39. *Microfluidic mixing: a review.* **Lee, C.-Y., Chang, C.-L., Wang, Y.-N. and Fu, L.-M.,.** 5, s.l. : Molecular Diversity Preservation International, 2011, International journal of molecular sciences, Vol. 12.
40. *Continuous flow microfluidic bioparticle concentrator.* **Martel, J. M., Smith, K. C., Dlamini, M., Pletcher, K., Yang, J., Karabacak, M., Haber, D. A., Kapur, R. and Toner, M.** s.l. : Nature Publishing Group, 2015, Scientific reports, Vol. 5, p. 11300.
41. *Optical and non-optical methods for detection and characterization of microparticles and exosomes.* **Van Der Pol, E, Hoekstra, AG., Sturk, A., Otto, C., Van Leeuwen, TG and Nieuwland, R.** 12, s.l. : Wiley Online Library, 2010, Journal of Thrombosis and Haemostasis, Vol. 8, pp. 2596-2607.

42. *Circulating tumor cell technologies.* **Ferreira, M., M., Ramani, V., C. and Jeffrey, S., S.** 3, s.l. : Elsevier, 2016, Molecular oncology, Vol. 10, pp. 374-394.
43. **Malvern Instruments.** *Mastersizer 2000 - user manual.* MAN0384-1.0. s.l. : Malvern Instruments Ltd. 2007, 2007.
44. *ImageJ2: ImageJ for the next generation of scientific image data.* **Rueden, C. T., Schindelin, J., Hiner, M. C., DeZonia, B. E., Walter, A. E., Arena, E. T., and Eliceiri, K. W.** s.l. : Springer Nature, 2017, BMC Bioinformatics, Vol. 18.
45. *Fiji: an open-source platform for biological-image analysis.* **Schindelin, J., Arganda-Carreras, I., Frise, E., Kaynig, V., Longair, M., Pietzsch, T., Preibisch, S., Rueden, C., Saalfield, S., Schmid, B., Tinevez, J.-Y., White, D., J., Hartenstein, V., Eliceiri, K., Tomancak, P. and Cardona, A.** 7, s.l. : Nature America, Inc, 2012, NAtUre MethOds, Vol. 9, p. 677.
46. **MicroMedicine, Inc.** MicroMedicine homepage. [Online] https://www.micromedicine.com/.
47. *Microfluidic devices in the fast-growing domain of single-cell analysis.* **Khan, M., Mao, S., Li, W., and Lin, J-M.** 58, s.l. : Wiley Online Library, 2018, Chemistry--A European Journal, Vol. 24, pp. 15398-15420.

Appendix A: ImageJ particle analysis images and coremacro

Examples of Optical Microscopy image (Figure 58) used to determine the particle counts and ratios in solutions and processed image in Figure 59.

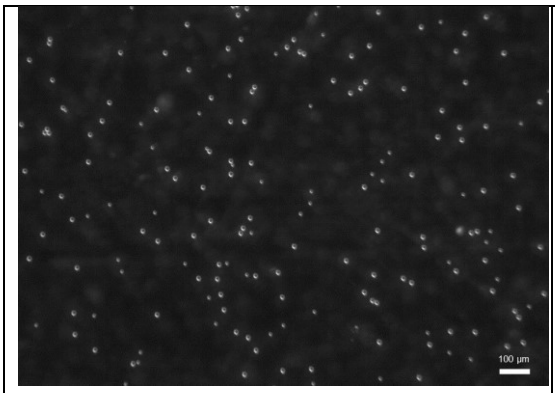

Figure 58 Dark field 5x image of 10 µm and 15 µm particles in DIW between two microscope slide. Sample from Labyrinth chip Inner outlet using 2.5 ml/min.

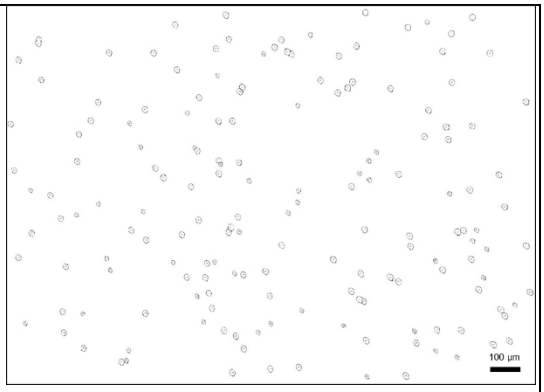

Figure 59 Processed with Fiji to obtain count of particles in Figure 58.

Coremacro used for particle analysis. Batches of images needed changing of brightness/contrast and colour thresholds:

```
run("Set Scale...", "distance=3 known=1 pixel=1 unit=µm global");
run("Set Measurements...", "area perimeter fit redirect=None decimal=3");
//run("Brightness/Contrast...");
setMinAndMax(17, 218);
run("Apply LUT");
setAutoThreshold("Default dark");
//run("Threshold...");
setThreshold(67, 255);
setOption("BlackBackground", true);
run("Convert to Mask");
run("Fill Holes");
run("Watershed");
run("Analyze Particles...", "size=50-200 circularity=0.30-1.00 show=Outlines display exclude clear summarize");
run("Distribution...", "parameter=Area or=5 and=0-0");
```

Appendix B: Tables of average particle counts

Here are presented the tables of the particle counts during experiments.

Table 5 Labyrinth chip Count of particles from average number of nine images in three different droplets.

Labyrinth chip					Spiral chip				
Flow rate		Test number average of 3 droplets			Flow rate		Test number average of 3 droplets		
1,75 ml/min		1	2	3	5 ml/min		1	2	3
Inner	10 µm count	46.3	3.0	69.0	Inner	10 µm count	242	257	375
	15 µm count	6.0	5.0	88.7		15 µm count	328	285	439
Middle	10 µm count	20.3	54.0	3.3	Middle	10 µm count	32.3	46.3	44.3
	15 µm count	22.3	57.0	2.3		15 µm count	43.7	43.3	17.3
Outer	10 µm count	18.7	0.7	0.3	Outer	10 µm count	1.7	4.7	1.3
	15 µm count	14.3	1.0	0.0		15 µm count	0.7	3.7	0.3
Flow rate		Test number average of 3 droplets			Flow rate		Test number average of 3 droplets		
2,5 ml/min		1	2	3	7 ml/min		1	2	3
Inner	10 µm count	66.0	115	130	Inner	10 µm count	209	54.0	156
	15 µm count	15.3	65.3	187		15 µm count	169	22.0	78.7
Middle	10 µm count	20.7	10.3	7.3	Middle	10 µm count	107	280	237
	15 µm count	20.0	45.0	22.7		15 µm count	236	416	352
Outer	10 µm count	2.3	3.0	1.3	Outer	10 µm count	197	14.7	5.3
	15 µm count	2.0	3.0	4.3		15 µm count	148	28.3	15.3
Flow rate		Test number average of 3 droplets			Flow rate		Test number average of 3 droplets		
3,25 ml/min		1	2	3	9 ml/min		1	2	3
Inner	10 µm count	3.3	95.7	41.0	Inner	10 µm count	62.3	18.3	15.0
	15 µm count	2.0	121	192		15 µm count	30.7	17.0	22.0
Middle	10 µm count	13.7	1.3	52.3	Middle	10 µm count	224	193	232
	15 µm count	26.3	2.3	49.0		15 µm count	249	281	361
Outer	10 µm count	29.7	0.3	16.7	Outer	10 µm count	167	129	142
	15 µm count	21.0	0.3	2.3		15 µm count	270	120	84.0

Concentrator chip				
Flow rate		Test number average of 3 droplets		
		1	2	3
0,35 ml/min	Product	3.7	34.7	17.3
	Waste	14.7	28.0	26.3
0,5 ml/min	Product	122.7	102.7	45.3
	Waste	9.0	6.3	19.0
0,65 ml/min	Product	98.3	81.3	47.7
	Waste	8.7	17.7	15.7

Appendix D: Table of cell counts

Here are presented the averages of cell counts in nine images in Table 6.

Table 6 Average counts of cells in 10x and 5x optical microscopic images and normalized cell counts.

			5x per 9 images				5x per 9 images
Medium 10^5	21.8. 16.45		4.3	PBS 5*10^4	23.8. 18.57		0.9
Medium 10^5	27.8. 14.43		1.2	PBS 5*10^4	24.8. 19.38		2.0
Spiral	5 ml/min	Inner	4.0	Spiral	5 ml/min	Inner	0.8
	21.08. 16.57	Middle	4.6		23.08. 19.11	Middle	1.4
		Outer	1.7			Outer	0.6
	7 ml/min	Inner	0.2		7 ml/min	Inner	0.1
	21.8. 18.11	Middle	1.7		24.8. 16.35	Middle	1.0
		Outer	3.9			Outer	2.0
	9 ml/min	Inner	0.2		9 ml/min	Inner	0.6
	22.8. 13.27	Middle	0.1		24.8. 17.38	Middle	0.3
		Outer	3.9			Outer	1.6
Labyrinth	1,75 ml/min	Inner	0.6	Labyrinth	1,75 ml/min	Inner	3.0
	22.8. 14.42	Middle	5.6		24.8. 20.15	Middle	2.8
		Outer	1.8			Outer	0.2
	2,5 ml/min	Inner	0.3		2,5 ml/min	Inner	1.0
	22.8. 18.08	Middle	10.6		24.8. 21.23	Middle	1.0
		Outer	1.6			Outer	0.2
	3,25 ml/min	Inner	0.1		3,25 ml/min	Inner	0.4
	22.8. 18.50	Middle	1.3		24.8. 21.59	Middle	0.1
		Outer	3.4			Outer	1.0
				PBS 10^4	27.8. 16.37		1.9
Conc	0,35 ml/min	Product	2.1	Conc	0,35 ml/min	Product	1.6
	23.8. 17.13	Waste	0.7		27.8. 18.55	Waste	0.2
	0,5 ml/min	Product	0.9		0,5 ml/min	Product	0.2
	23.8. 16.18	Waste	1.1		27.8. 18.40	Waste	0.1
	0,65 ml/min	Product	0.3		0,65 ml/min	Product	0.3
	27.8. 15.14	Waste	0.8		27.8. 19.16	Waste	0.2